www.sciencemag.org/content/358/6360/eaam5690/suppl/DC1

Supplementary Materials for

Contrasting carbon cycle responses of the tropical continents to the 2015–2016 El Niño

Junjie Liu,* Kevin W. Bowman, David S. Schimel, Nicolas C. Parazoo, Zhe Jiang, Meemong Lee, A. Anthony Bloom, Debra Wunch, Christian Frankenberg, Ying Sun, Christopher W. O'Dell, Kevin R. Gurney, Dimitris Menemenlis, Michelle Gierach, David Crisp, Annmarie Eldering

*Corresponding author. Email: junjie.liu@jpl.nasa.gov

This PDF file includes:

Materials and Methods
Supplementary Text
Figs. S1 to S13
Table S1
References

Materials and Methods

Oceanic Nino Index

One of the indictors to represent the magnitude of positive phase (i.e., El Niño) and negative phase (i.e., La Niña) of El Niño Oscillation (ENSO) is Oceanic Nino Index (ONI). It is defined as the sea surface temperature anomaly over Nino 3.4 region (5°N-5°S, 120°-170°W). When ONI is larger than 0.5, it is El Niño; while it is La Niña when ONI is smaller than -0.5. Figure S1 shows the ONI from Aug 2014 to Dec 2016, which indicates that the El Niño conditions started at the end of 2014 and lasted till May 2016.

GPP-weighted precipitation and land surface temperature

The precipitation data is from the NOAA Climate Predication Center Merged Precipitation Analysis (CMAP) (*82*) (https://www.esrl.noaa.gov/psd/data/gridded/data.cmap.html), which starts from 1979 and continues until the present. The surface skin temperature is from ERA-interim reanalysis (*83*). Inspired by the weighting method used in (*84*), we weight the monthly mean precipitation and surface skin temperature at each grid point *i* with the 2011 monthly mean CASA-GFED3 (*85*) Gross Primary Production (GPP) (http://nacp-files.nacarbon.org/nacp-kawa-01/?C=M;O=D) to calculate the GPP-weighted annual mean values:

$$z_{i,iyear} = \frac{\sum_{t=Jan}^{t=Dec(iyear)} v_{i,t} g_{i,t}}{\sum_{t=Jan(iyear)}^{Dec} g_{i,t}} \qquad (1)$$

where $v_{i,t}$ represents either precipitation or temperature. The quantity $z_{i,iyear}$ is the final GPP-weighted annual mean value for a specific year *iyear* at grid point *i*. By weighting the physical climate states with GPP, the annual mean values weight more strongly over the months when the

vegetation is more active. When calculating a regional mean value, the grid points with more active vegetation also have larger weights.

Figure S2 is the 36-year time series of GPP-weighted precipitation (top) and temperature (bottom) over tropical South America (left), tropical Africa (middle), and Tropical Asia (right). The grey line is the 30-year (1981-2010) mean, while the green bar is 2 σ over the 30 years (1981-2010). Year 2015 is an anomalous warmer and drier year compared to the climatology over the three tropical regions. Over tropical South America, the annual mean precipitation is the lowest in 35 years; about 2.1 σ lower than the climatology mean. Over tropical Africa, the temperature is about 1.0 σ higher than the mean state. The annual mean precipitation over tropical Asia is 1.7 σ lower than the climatology mean, but it is slightly higher than the annual mean precipitation in the other two "very strong" El Niño years: 1982 and 1997.

OCO-2 X_{CO2} observations

The OCO-2 provides global coverage with a 16-day repeat cycle and three operational modes: nadir, glint, and target. Both nadir and glint observations are observed over land, and only glint observations are observed over ocean. We find that the relative bias between land nadir and land glint observations is about 0.3 ppm averaged over the globe in 2015 but the bias is spatially and temporally dependent (Figure S3), and the gradient between ocean glint observations and land nadir observations over outflow region is much higher than model simulated value (Figure S4). In order to avoid the impact of relative biases in different observation modes on flux estimations, we only use land nadir observations in this study. We further filter the observations based on the quality control flag provided along with the OCO-2 v7br lite product (*86*).

Figure S5 shows the 2015 annual total number of good quality land nadir observations at each $4°$ $\times 5°$ grid box. The amount of observations over semiarid regions, such as Australia and South Africa, is about 10 times more than the observations over other regions. The 4D-Var inversion process optimizes fluxes by minimizing the misfit between observations and the model simulated concentration. The minimizing process would be dominated by the contributions from these observations if we directly assimilate these observations without thinning or averaging. We adopt a two-step strategy to homogenize the observation spatial distribution and remove the outliers. We first do a buddy-check (87) to remove the outliers within a 100 km circular domain at the same orbit track. The observation y_i is removed if

$$\left| y_i - \frac{1}{n} \sum_{ii \in A} y_{ii} \right| > 2\sigma^o \qquad (2)$$

where A represents 100 km circular domain, n is the total number of observations within the domain, and ii is within the domain. The value σ^o is the standard deviation of all the observations within the domain. We then calculate a super observation (or "superobs") for every $1° \times 1°$ box by averaging the observations within the $1° \times 1°$ domain at the same orbit track. Note that the $1°$ $\times 1°$ box does not have overlaps. The mean latitude, longitude, and time are the longitude, latitude, and time of the new super observation. In calculating the model simulated X_{CO2} (y^b), we use the mean of the averaging kernels (A) (**A)**, the prior X_{CO2} ($x^{o(\text{column})}$) and prior CO2 profiles ($x^{o(\text{profile})}$) within the $1° \times 1°$ box of the same orbit track based on the following equation:

$$\mathbf{y}^b = \mathbf{x}^{o(column)} + \mathbf{A}^T \left(\mathbf{x}^{b(profile)} - \mathbf{x}^{o(profile)} \right) (3)$$

where $\mathbf{x}^{b(profile)}$ is model simulated CO2 profiles interpolated to observation time and space. Since each sounding from OCO-2 has a surface footprint of ~1.29 km $\times$ 2.25 km at nadir, while the

transport model resolution is much coarser, we not only reduce the random errors, but also reduce the model representation errors when averaging the observations. Figure S5 b shows the annual total assimilated observations at each $4° \times 5°$ box. After the two-step thinning and superobs production, the spatial distribution of observation coverage is much more homogeneous.

The observation error standard deviations used in the inversion process are the sum of the mean of the observation error statistics and the standard deviation of the observations within the $1° \times 1°$ box along the same orbit track. The standard deviation of the observations is used to approximate the model representation errors. The mean of the observation error statistics within the $1° \times 1°$ box are used to represent biases, assuming biases are dominant relative to random errors (*88*).

ACOS-GOSAT b3.5

We use ACOS-GOSAT b3.5 land nadir high-gain observations, and filter the observations with the quality control flag. Figure S5 c shows the total number of observations for year 2011. The ACOS-GOSAT b3.5 observations have been extensively validated (*89, 90*) and are publically available (https://co2.jpl.nasa.gov/#mission=ACOS). The record spans from April 2009 to June 2014. Compared to OCO-2 superobs, the number of ACOS-GOSAT is larger over some regions, which is due to the 3-day repeat cycle of GOSAT observations and the superobs step that we did for OCO-2 observations.

A framework to quantify and attribute the Net Biome Exchange (NBE) to constituent carbon fluxes

Figure S6 illustrates the framework we used to quantify and attribute the NBE to constituent carbon fluxes by assimilating multiple types of satellite observations. The land biosphere flux NBE $(F_{bio})_i$ at any grid point can be written as:

$$(F_{bio})_i = -g_i + s_i + r_i \quad (4)$$

where, g_i, s_i and r_i are GPP, biomass burning, and total ecosystem respiration at the same grid point. In the above equation, positive means releasing carbon into the atmosphere. The land net biosphere fluxes, GPP (g_i), and biomass burning (s_i) carbon fluxes were constrained with X_{CO2} from OCO-2 and GOSAT, Solar Induced Fluorescence (SIF) from GOSAT (31), and CO observations from MOPITT (34) separately (Figure S6). Once these quantities are calculated, respiration is calculated as a residual. The error variance of respiration is the sum of GPP, biomass burning, and land biosphere flux error variance. In the following, we describe the optimization methods for NBE (a), GPP (b) and biomass burning (c) individually.

(a) Inversion methodology and experiments used to optimize NBE

We use the Carbon Monitoring System Flux (CMS-Flux, 24-26) inversion framework to estimate monthly mean land and ocean fluxes assuming accurate fossil fuel emissions. The CMS-Flux optimizes surface fluxes with a 4D-Var approach with the GEOS-Chem adjoint model. The GEOS-Chem transport model and its adjoint are run at 4° × 5° resolution driven by GEOS-5 (64) (before year 2014) and GEOS-FP meteorology (after year 2014). A Monte Carlo approach is used to estimate the uncertainties of posterior fluxes at each grid. The regional posterior flux uncertainties are the standard deviations of the regionally aggregated ensemble posterior fluxes from the Monte Carlo method. The interested readers can refer to *(25)* for additional details of the inversion system.

We carry out two inversion experiments: one spans from December 2009 to December 2012 (exp-1), and the other spans from September 2014 to Dec 2016 (exp-2). The exp-1 assimilates ACOS-GOSAT b 3.5 X_{CO2} using the GEOS-5 meteorology, while exp-2 assimilates OCO-2 X_{CO2} using GEOS-FP. The prior fluxes include 3-hourly biosphere fluxes from CASA-GFED3 (*85*), 3-hourly ocean fluxes from ECCO2-Darwin (*91, 92*), and hourly fossil fuel emissions from Fossil Fuel Data Assimilation System (FFDAS) (*93*). Figure S7 is the annual mean prior biosphere flux uncertainty, which shows larger uncertainty over the tropics and regions with active biosphere activities.

In order to isolate the impact of prior fluxes on the posterior flux changes between year 2015 and 2011, we use the same prior biosphere fluxes and uncertainties for year 2011, and 2015-16 in exp-1 and exp-2. We show in the following that the posterior flux difference between 2011 and 2015-16 is independent of prior biosphere fluxes with our experimental setup. The posterior flux $\mathbf{x}^a$ can be written as:

$$\mathbf{x}^a = \mathbf{x}^b + \frac{\mathbf{P}^b\mathbf{H}^T}{\mathbf{H}\mathbf{P}^b\mathbf{H}^T + \mathbf{R}}\left(\mathbf{y} - h(\mathbf{x}^b)\right) \qquad (5)$$

where $\mathbf{x}^b$ and $\mathbf{P}^b$ are the prior flux and its uncertainty, and $\mathbf{R}$ is the observation error covariance. The observations and the model-simulated observations are represented by $\mathbf{y}$ and $h(\mathbf{x}^b)$ respectively, and $h(\cdot)$ is the observation operator. Since we use the same prior flux and uncertainties, the posterior flux differences between year 2015 and 2011 can be written as:

$$\Delta\mathbf{x}^a = \frac{\mathbf{P}^b\mathbf{H}_{2015}^T}{\mathbf{H}_{2015}\mathbf{P}^b\mathbf{H}_{2015}^T + \mathbf{R}_{2015}}(\mathbf{y}_{2015} - h(\mathbf{x}^b)) - \frac{\mathbf{P}^b\mathbf{H}_{2011}^T}{\mathbf{H}_{2011}\mathbf{P}^b\mathbf{H}_{2011}^T + \mathbf{R}_{2011}}(\mathbf{y}_{2011} - h(\mathbf{x}^b)) \qquad (6)$$

Assuming 2015 and 2011 X_{CO2} observations have similar sampling and observation error statistics, i.e., the linearized observation operator H, observation operator $h(\cdot)$ and $\mathbf{R}$ are similar, the posterior flux differences between year 2015 and year 2011 can be written as:

$$\Delta \mathbf{x}^{a} = \frac{\mathbf{P}^{b}\mathbf{H}^{T}}{\mathbf{H}\mathbf{P}^{T}\mathbf{H}^{T}+\mathbf{R}}\Delta \mathbf{y} \quad (7)$$

Therefore, the flux differences are only due to the differences in the observed CO_2 that were projected to the flux space with the sensitivity of observations to surface fluxes, the prior biosphere flux uncertainty, and the observation uncertainties. The impact of different observation sampling and observation error statistics on flux differences between 2015 and 2011 are addressed in *Supplementary Text*.

The CO2 annual growth rate at any given year t is the sum of the spatially distributed surface fluxes:

$$C_{a}^{t} = \sum_{i\in globe} ((F_{ff})_{i}^{t}+(F_{bio})_{i}^{t}+(F_{ocn})_{i}^{t}) \quad (8)$$

where $(F_{ff})_{i}^{t}$, and $(F_{ocn})_{i}^{t}$ are the fossil fuel emissions and ocean fluxes at point i for year t. The atmospheric inversion process optimizes surface fluxes so that they agree with the observed CO2 growth rate. The changes of CO2 growth rate between two years ΔC_{a} can be expressed as the sum of spatially resolved flux changes between these two years:

$$\Delta C_{a} = C_{a}^{t_{2}} - C_{a}^{t_{1}} = \sum_{i\in globe} \left[\Delta(F_{ff})_{i}^{t_{2}-t_{1}}+\Delta(F_{bio})_{i}^{t_{2}-t_{1}}+\Delta(F_{ocn})_{i}^{t_{2}-t_{1}} \right] \quad (9)$$

where $C_{a}^{t_{2}}$ and $C_{a}^{t_{1}}$ are the atmospheric CO2 growth rate for year t_2 and t_1 respectively, and $\Delta(F_{bio})_{i}^{t_{2}-t_{1}}$ is the contribution of biosphere flux changes at grid point i to the changes of global CO2 growth rate between year t_2 and t_1. Equation (9) can be further written as:

$$\sum_{i\in globe} \left[\Delta(F_{bio})_{i}^{t_{2}-t_{1}}\right] = \Delta C_{a} - \sum_{i\in globe} \left[\Delta(F_{ff})_{i}^{t_{2}-t_{1}}+\Delta(F_{ocn})_{i}^{t_{2}-t_{1}}\right] \quad (10)$$

Therefore, the posterior biosphere flux differences between year 2015 and 2011 are only due to the differences in the observed CO2 growth rate, with the assumption that the fossil fuel and the posterior ocean fluxes are much more accurate than the biosphere fluxes and the variability are much smaller, which is generally the case in tropical land regions (*94*).

(b) GOSAT-SIF optimized GPP

We use a Bayesian analysis framework to estimate monthly average GPP at 4º x 5º grid spacing (consistent with CMS-Flux grid) that optimally accounts for uncertainties in predictions of GPP from terrestrial biosphere models, satellite observations of GOSAT SIF, and relationships between SIF and GPP (*32*). Monthly prior GPP is predicted from the average of 10 land biosphere models (CLM4.5, ISAM, JULES, LPJG, LPJ, LPX, OCN, ORCHIDEE, VEGAS, VISIT) from the TRENDY model intercomparison project over the period 2009-2012 (http://dgvm.ceh.ac.uk/node/9) (*95*), and temporally downscaled to daily resolution using year specific downward shortwave radiation from the NCEP reanalysis dataset (*96*), which is provided by the NOAA/OAR/ESRL PSD, Boulder, Colorado, USA, from their Web site at http://www.esrl.noaa.gov/psd/. Figure S8a shows the prior GPP uncertainty estimated as the spread of TRENDY models. The annual prior GPP over tropical South America, tropical Africa and Asia are 20.6, 18.1, and 10.4 GtC/year respectively, while the prior uncertainties are 1.5, 1.7 and 1.1 GtC/year respectively. The prior GPP uncertainties range from 7% to 11%.

GOSAT-SIF from Level 2 product was scaled to monthly GPP using the empirical linear relationship with Max Planck Institute (MPI) GPP from 2009-2011 with careful accounting for uncertainties in SIF measurements and the MPI approach (*32, 33*). MPI GPP is derived from a flux

tower data based upscaling approach using the Max Planck Institute for Biogeochemistry (MPI-BGC) model. The posterior GPP and uncertainties are calculated with least square linear combination of the scaled SIF observations and the prior GPP based on their uncertainties. This approach has been used to examine large-scale GPP distributions and regional GPP responses to climate variability and drought, and has been extensively validated against flux tower data (*33*). The combination of optimized GPP and uncertainty in this study provides a regional semi-empirical GPP constraint, helps to quantify the significance of regional GPP changes, and provides a range of uncertainty for determining the significance of predicted GPP. The posterior GPP changes between 2015 and 2011 are only due to the assimilation of year specific satellite SIF data, since the prior information is the same between two years. The posterior uncertainty reduction (Figure S8b) can be as large as 60% where observational coverage and prior uncertainty are high. The posterior uncertainties over tropical South America, tropical Africa and Asia are 0.6, 0.7, and 0.6 GtC/year respectively for 2015. The uncertainty reduction is 30 to 60% over most of the tropical regions.

(c) Quantification of biomass burning carbon fluxes

The carbon fluxes from biomass burning are estimated as a multiplication between CO2:CO emission ratio and the CO carbon fluxes optimized with MOPITT v6 CO observations. The CO emission optimization follows (*35*), which optimize monthly CO emissions independently with initial conditions for each month estimated from a sub-optimal Kalman filter (*65*). The CO2:CO emission ratio ($r_{CO2:CO}$) at each grid point is calculated using CO2 and CO emission factors (e_{co_2}, e_{co}) and dry mass matter (m_v) for six vegetation types used in GEOS-Chem:

$$r_{CO2:CO} = \frac{\sum_{i=1}^{6}(e_{CO_2})_i \cdot m_i}{\sum_{i=1}^{6}(e_{CO})_i \cdot m_i} \quad (11)$$

where i represents vegetation types that include agriculture waste, deforestation, extra-tropical forest, peat, savanna, and woodland. The emission ratio for peat fire over Indonesia is based on field measurement from (36). We carry out six-year inversion from 2010 to 2015. The uncertainty of the posterior biomass fluxes is based on Monte Carlo method (25).

Supplementary Text
Is there any relative bias between OCO-2 and ACOS-GOSAT X_{CO2}?

Since we contrast the 2015 posterior biosphere flux constrained by OCO-2 XCO2 observations against 2011 biosphere flux constrained by ACOS-GOSAT XCO2 to discuss the sensitivity of tropical land biosphere carbon fluxes to warmer and drier conditions resulted from the 2015 El Niño, in this section we address whether there is relative bias between OCO-2 and ACOS-GOSAT b3.5 XCO2. We compare the XCO2 observations from OCO-2 and ACOX-GOSAT b3.5 against XCO2 observations from the total Column Carbon Observing Network (TCCON) (30). Figure S9 shows the comparison of 2015 OCO-2 land nadir XCO2 observations and 2011 ACOS-GOSAT land high gain XCO2 observations against observations from the same 14 TCCON sites (67-81). It shows that the OCO2 land nadir observations and ACOS-GOSAT land high gain observations have the similar slope relative to TCCON observations, which are 0.79±0.04 and 0.76 ±0.03 respectively for OCO-2 and ACOS-GOSAT. The overall bias between ACOS-GOSAT and TCCON in 2011 is 0.34 ppm, whereas the overall bias between OCO-2 and TCCON in 2015 is 0.38 ppm (81). The similar biases exclude the possibility of the propagation of relative biases between OCO-2 and ACOS-GOSAT into the posterior flux differences.

Do the different samplings and observation error statistics between OCO-2 and ACOS-GOSAT affect the posterior biosphere flux differences between 2015 and 2011?

We address the impact of sampling and observation error statistics on flux inversion results by carrying out two Observing System Simulation Experiments (OSSE). The two inversion experiments use the same prior fluxes and nature run that is used to create simulated observations. The differences between the two inversion experiments are the sampling of the simulated observations and the observation error statistics. Therefore, the differences in posterior fluxes from these two OSSEs are due to the impact of different sampling and observation error statistics between OCO-2 and ACOS-GOSAT. The inversion experiments span two years.

Figure S10 shows the two-year "true" fluxes (black), prior (blue), and posterior fluxes and their uncertainties optimized with OCO-2 sampling (red) and ACOS-GOSAT sampling (green) over three tropical regions. It shows that the prior fluxes and true fluxes have different seasonal cycles, but the posterior fluxes from both the OCO-2 and ACOS-GOSAT inversion experiments are much closer to the true fluxes, and the differences are within the monthly posterior flux uncertainty estimates. Based on OCO-2 sampling and observation error statistics, the annual estimated posterior fluxes are 0.6 ± 0.17, -1.4 ± 0.13, -0.3 ± 0.18 for tropical South America, Africa, and Asia respectively; while based on ACOS-GOSAT sampling and observation error statistics, the annual estimated posterior fluxes are 0.6 ± 0.17, -1.5 ± 0.13, -0.4 ± 0.20 respectively for the three tropical continents. The differences are within the uncertainty estimates. Therefore, the posterior biosphere flux differences between 2015 and 2011 are resulted from the imprint of 2015 El Niño

and 2011 La Niña events on CO2 concentration differences, but not from the different samplings and observation error statistics between OCO-2 and ACOS-GOSAT.

The atmospheric CO₂ growth rate and airborne fraction estimation

In 2015, the NOAA observed atmospheric CO2 growth rate is 6.30 ± 0.20 GtC (*S42*). Assimilating OCO-2 X_{CO2} observations and using the 2011 prior biosphere fluxes, we estimate 6.41 ± 0.64 GtC total atmospheric CO2 growth rate (Table S1), consistent with the NOAA flask observations. In contrast, the total atmospheric CO2 growth rate based on NOAA flask observations is 3.58 ± 0.20 GtC in 2011 (*19*). Assimilating ACOS-GOSAT observations, we estimate 3.46 ± 0.65 GtC total atmospheric CO2 growth rate (Table S1), consistent with the observed value. The atmospheric CO2 air borne ratio, the ratio between the atmospheric CO2 growth rate and the sum of fossil fuel emissions and land use land change (*18*), is 0.56 in 2015 vs. 0.34 in 2011 (Table S1).

The difference between fossil fuel emissions and atmospheric CO2 growth rate is the amount absorbed by ocean and land (Table S1). The ocean flux difference between these two years is only 0.2 GtC, much smaller than the posterior biosphere flux differences, which is consistent with the smaller ocean flux variability discussed in previous studies (*94*). In 2015, the posterior land biosphere flux is -0.47 ± 0.53, while it is -3.46 ± 0.59 in 2011. The estimated 3.0 GtC atmospheric

CO2 growth rate difference between 2015 and 2011 is almost entirely due to the changes of land biosphere fluxes between these two years.

Validation of posterior CO2 concentrations against independent aircraft observations and surface flask observations

We validate the posterior CO2 concentrations from the two inversion experiments against independent aircraft and surface flask observations, which are from Observation Data Package (ObsPack) product (*66, 97*). Figure S11 shows the aircraft and surface flask CO2 observation coverage for year 2011 and year 2015. Most of the aircraft observations are over North America (NA), and most of the surface flask observations are over the Northern hemisphere (NH). Figure S11 shows the CO2 vertical profiles from aircraft observations (black), the prior (blue), and the posterior (red) sampled at the aircraft locations and time averaged over year 2001 (left column) and 2015 (right column). Figure S13 shows the CO2 time series of surface flask CO2 observations (black), and prior (blue) and posterior (red) CO2 concentrations sampled at surface flask locations and time. For both years, the posterior CO2 concentrations are more accurate than the prior CO2 concentrations compared to both aircraft and surface flask observations. Relative to aircraft observations (Figure S 12), the global mean root mean square (RMS) error of the 2011 posterior CO2 concentration is 0.27 ppm, while the RMS error of the prior CO2 concentration is 1.14 ppm. The RMS error of the 2015 posterior CO2 concentration is 0.41 ppm, while the RMS error of the prior CO2 concentration is 1.76 ppm. Relative to surface flask observations (Figure S12), the global mean RMS error changes from 2.18 ppm to 1.67 ppm after assimilating ACOS-GOSAT for 2011, and changes from 2.51 ppm to 0.81 ppm after assimilating OCO-2 XCO2 for year 2015.

Monthly time series of Oceanic Nino Index (ONI) from Aug 2014 to Dec 2016
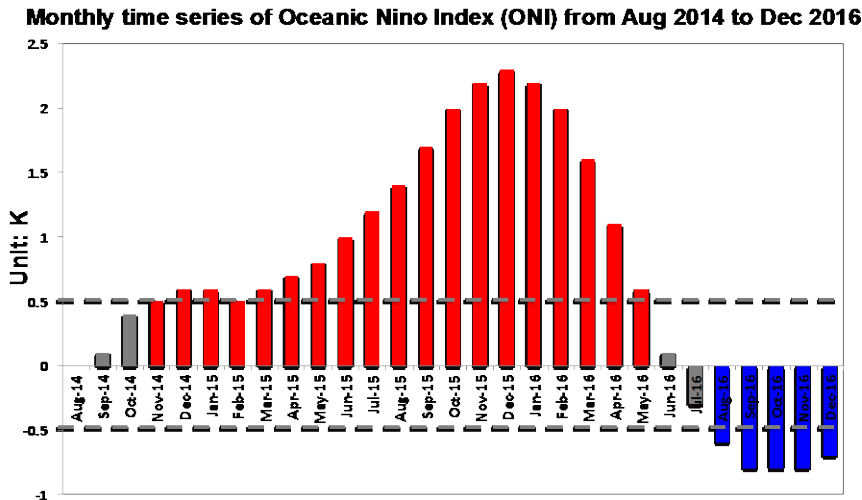

Figure S1 Monthly time series of Oceanic Nino Index (NOI) from Aug 2014 to Dec 2016. NOI is defined as Sea Surface Temperature (SST) anomaly over Nino 3.4 region. The data is from http://www.cpc.ncep.noaa.gov/products/analysis_monitoring/ensostuff/ensoyears.shtml. Red bars indicate El Niño condition, when SST anomaly is larger than 0.5 K, while blue bars indicate La Niña condition, when SST anomaly is lower than -0.5 K.
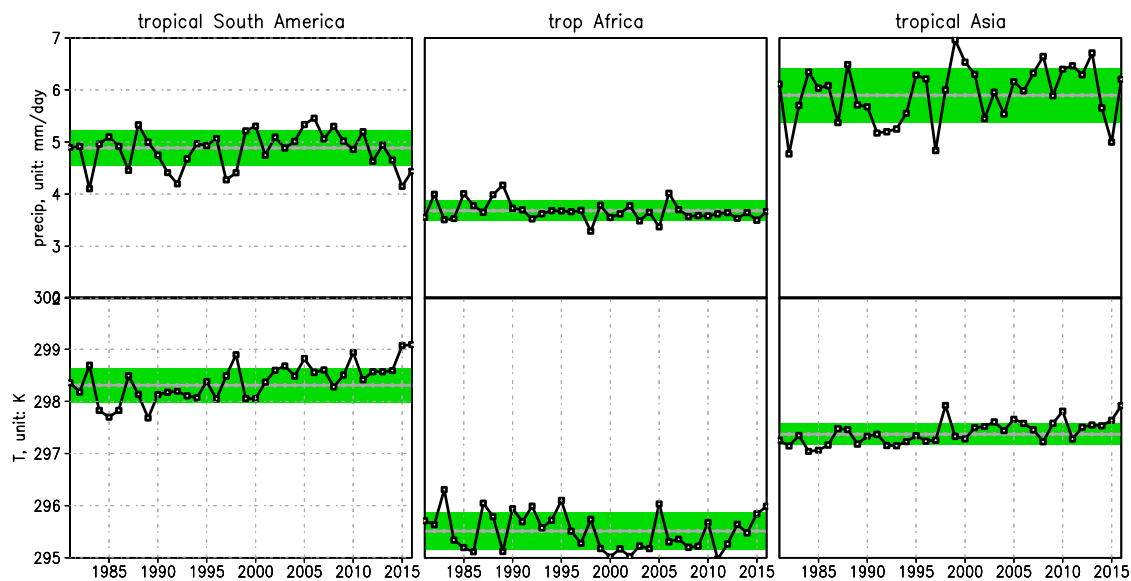
Figure S2 Times-series of GPP-weighted precipitation (top row) (unit: mm/day) and temperature (bottom row) (unit: K) over tropical South America (left), tropical Africa (middle), and tropical Asia (right) from 1981 to 2016. The grey line in each plot is the 30-year (1981-2010) mean for the corresponding variable at the corresponding region. The green bar in each plot is 2 σ over 30 years (1981-2010).
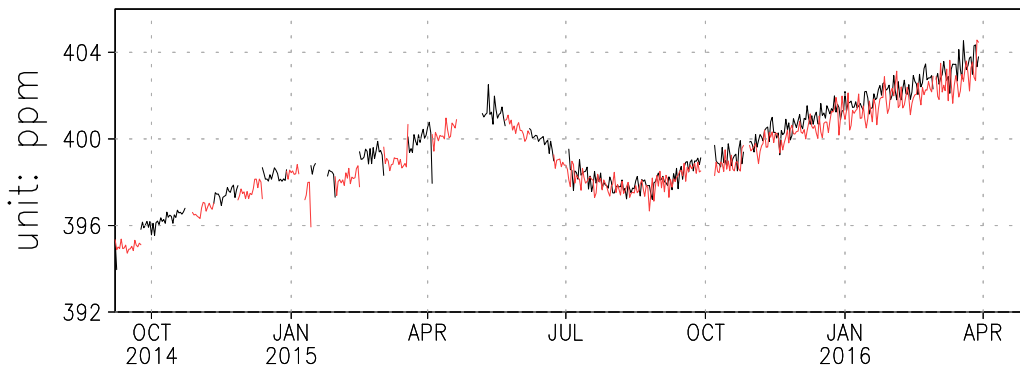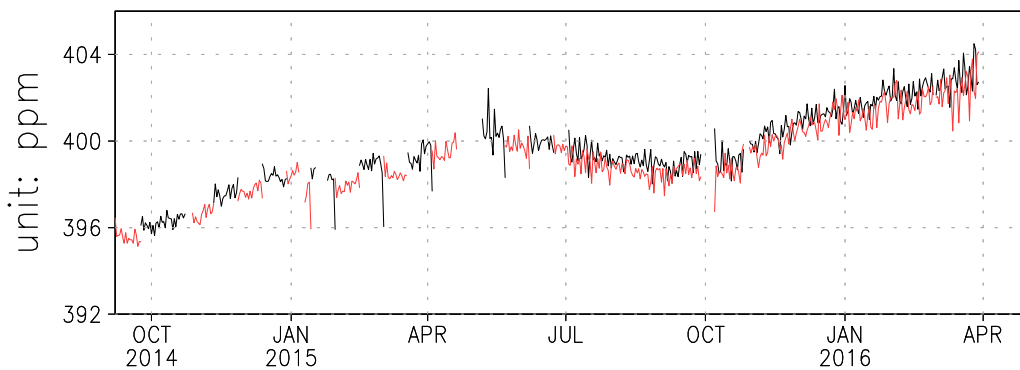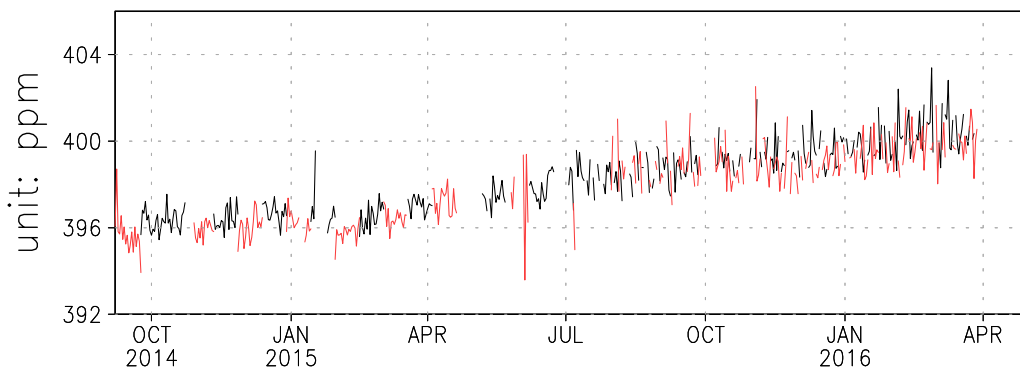
Figure S3 OCO-2 land nadir observations (black) and land glint observations (red) averaged over the globe (a), 30°S-30°N (b), 60°S-30°S(c). The region mean differences between land nadir and land glint observation are 0.33 ppm, 0.39 ppm, and 0.66 ppm respectively averaged over the globe, 30°S-30°N, and 60°S-30°S.
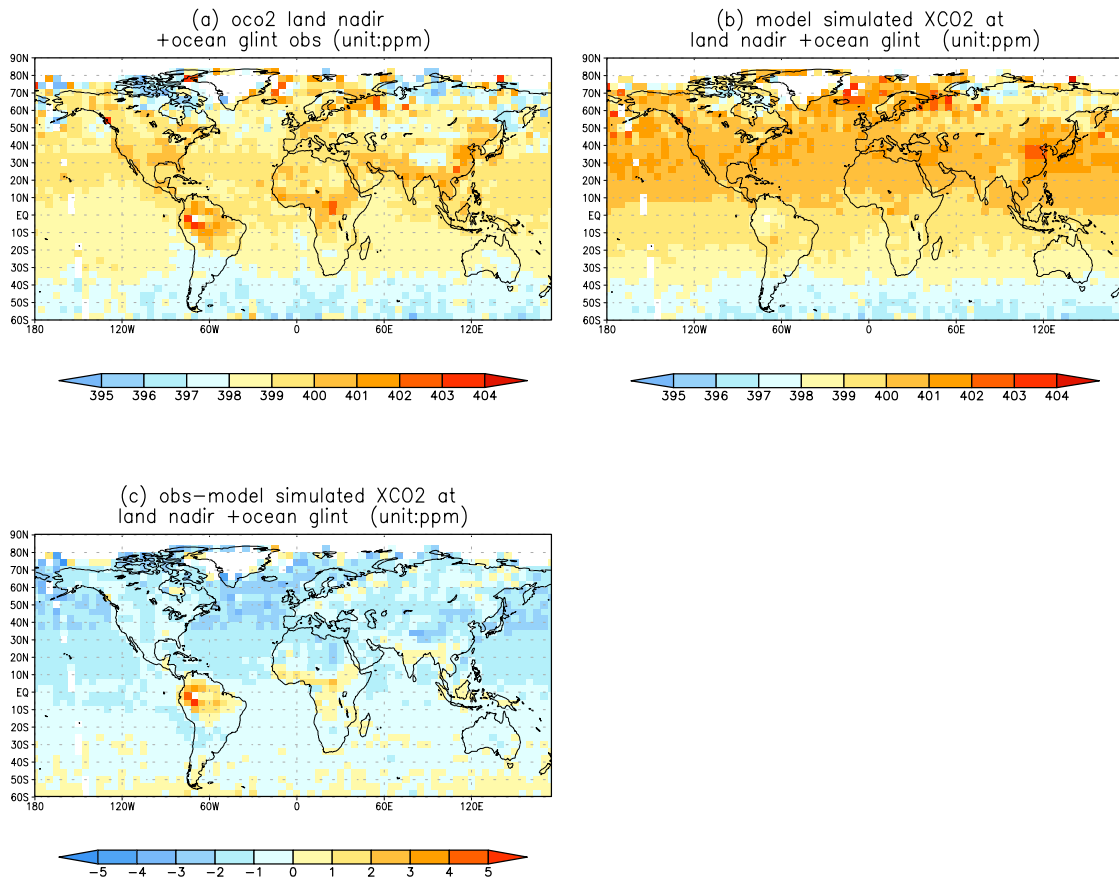
Figure S4 (a) 2015 annual mean OCO-2 land nadir and ocean glint observations; (b) model simulated XCO2 sampled with OCO-2 averaging kernels at land nadir and ocean glint locations; (c) The differences between OCO-2 observations and model simulated XCO2. Unit: ppm.
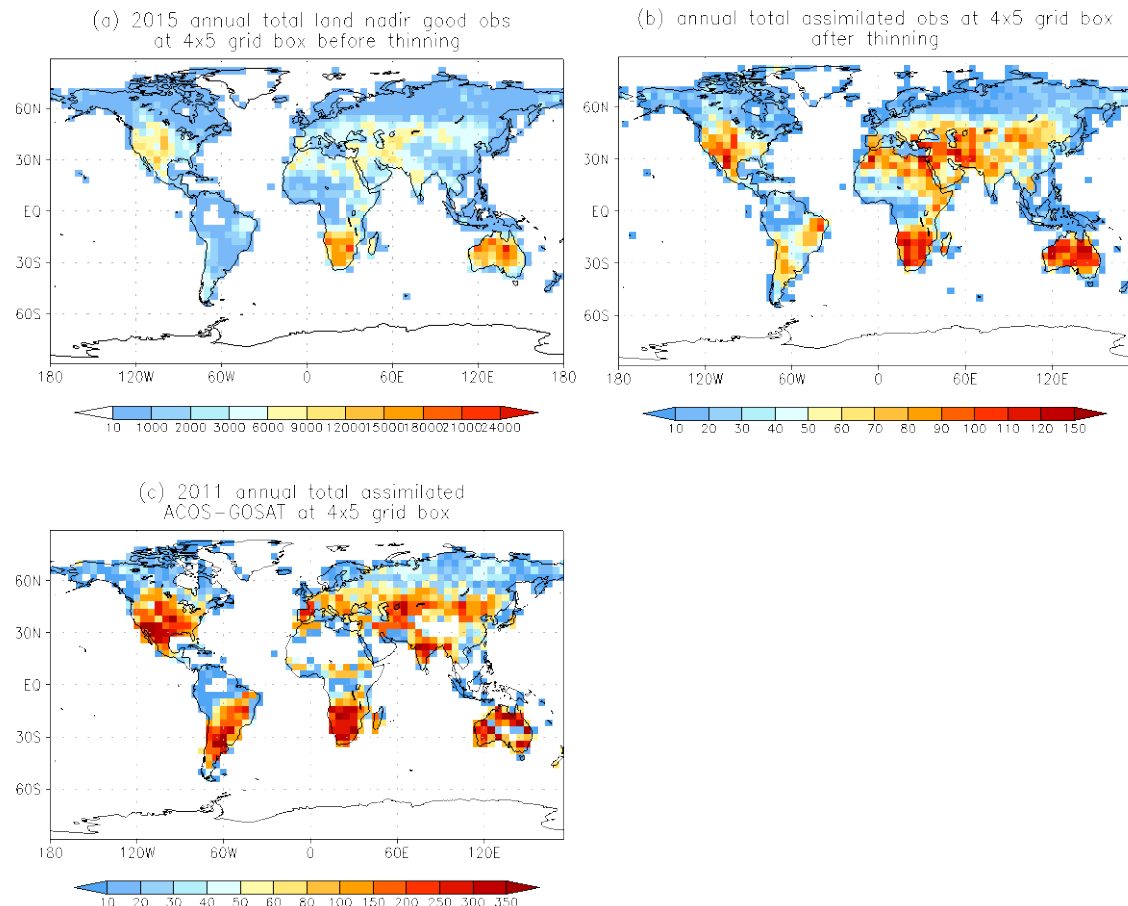
Figure S5 a. The 2015 annual total land nadir good quality observations at each 4° x 5° grid point before thinning; b. The annual total OCO2 observations at each 4° x 5° grid point after thinning; c. 2011 annual total assimilated ACOS-GOSAT b3.5 observations at each 4° x 5° grid point.
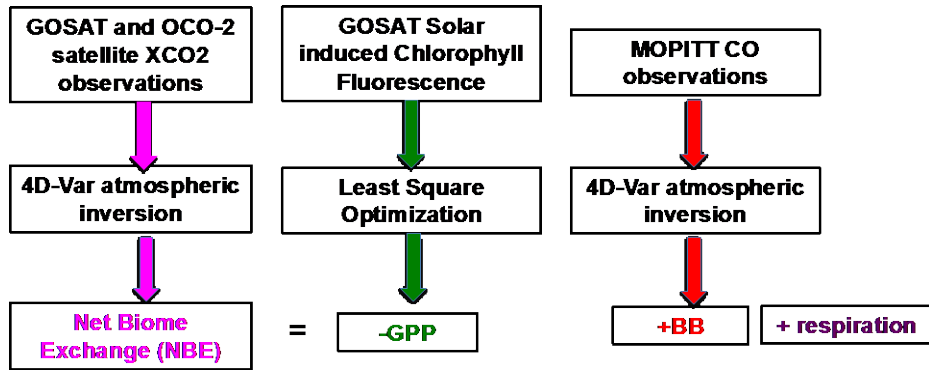
Figure S6 A framework to constrain net biome exchange (NBE) and its constituent fluxes including GPP and biomass burning.

**Figure S7 Annual mean prior biosphere flux uncertainty (unit: gC/m²/day)**

(a) prior GPP uncertainty (GtC/yr)

## (b) GPP posterior uncertainty reduction (%)
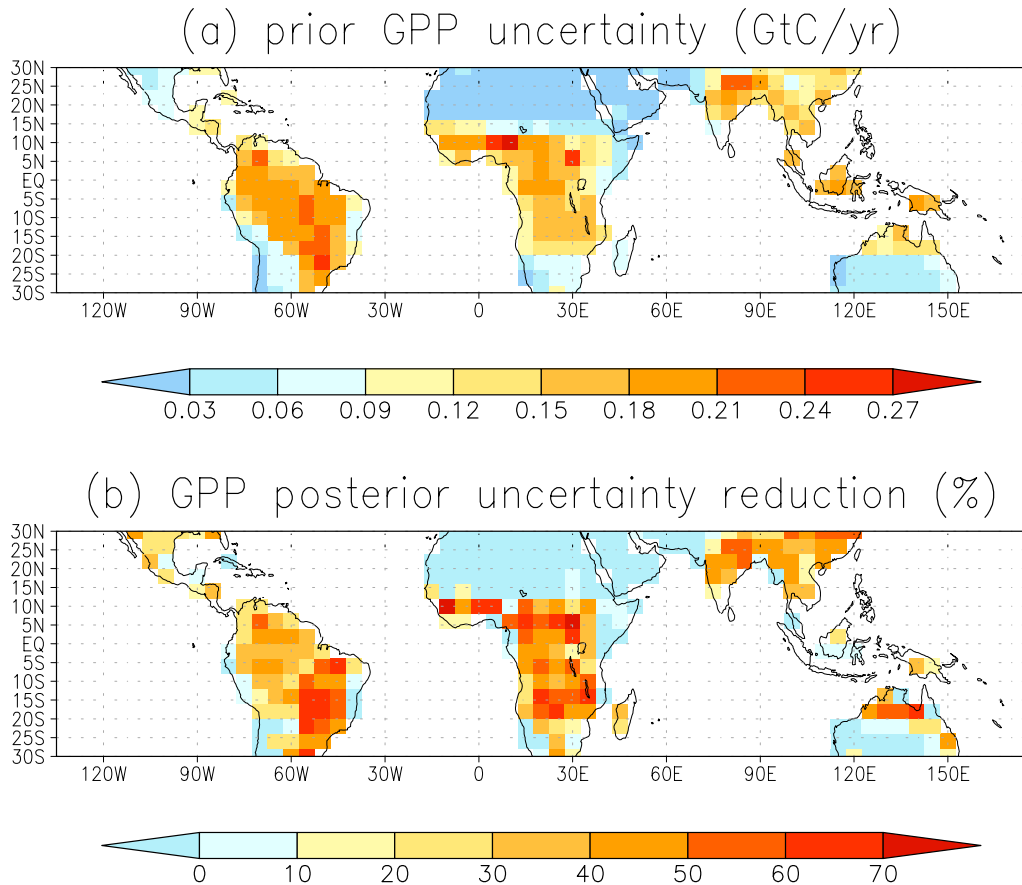
Figure S8 (a) The prior annual GPP uncertainty (unit: GtC/year), and (b) the GPP posterior uncertainty reduction (unit: %).
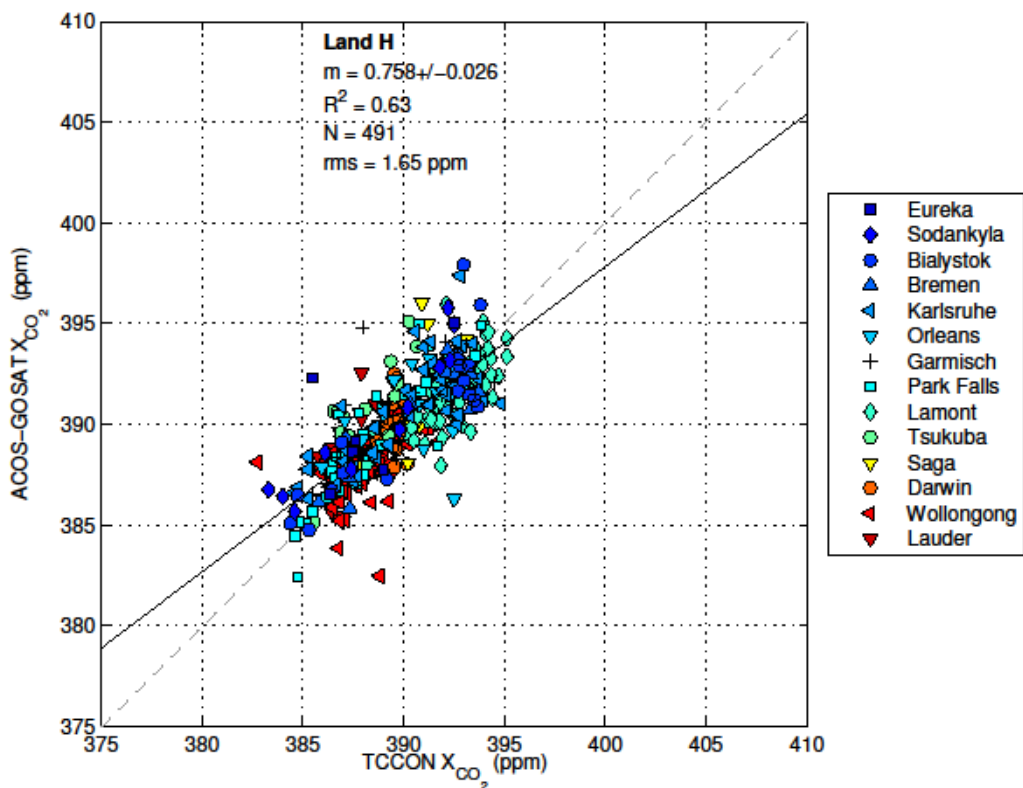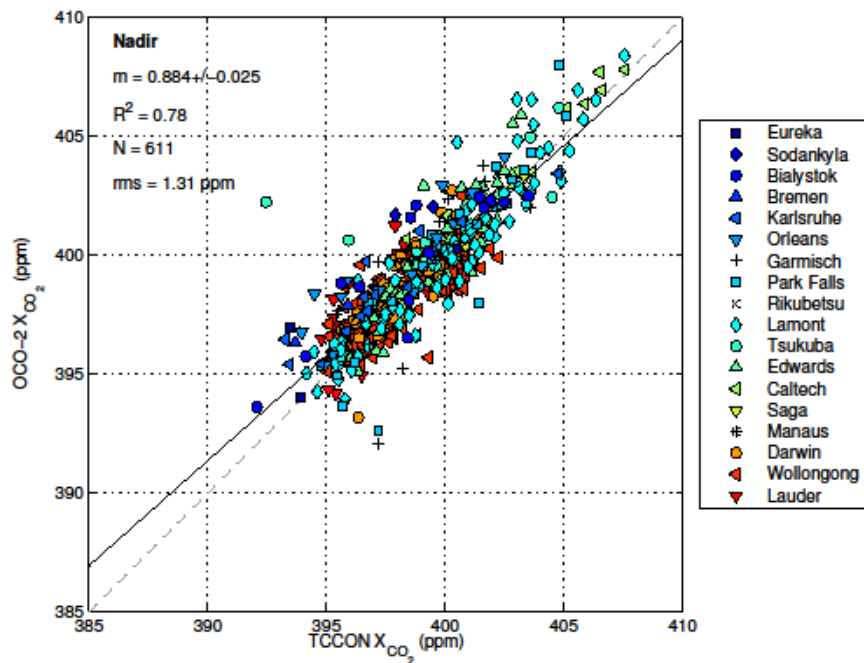
Figure S9 Comparison of OCO-2 2015 land nadir XCO2 observations and 2011 ACOS-GOSAT b3.5 land high gain XCO2 observations with TCCON observations. Top panel: 2015 OCO2 XCO2 vs. TCCON; bottom panel: 2011 ACOS-GOSAT XCO2 vs. TCCON. The slope between 2015 OCO2 XCO2 and TCCON is 0.790 ±0.041, while the slope between 2011 ACOS-GOSAT XCO2 and TCCON is 0.758 ±0.026. The root mean square differences are 1.45 ppm and 1.65 ppm respectively for 2015 OCO2 XCO2 and 2011 ACOS-GOSAT XCO2.

(a) trop South America,black: truth; blue: prior;
red: post−oco2;green: post−gosat

(b) trop Africa,black: truth; blue: prior;
red: post−oco2;green: post−gosat

(c) trop Asia,black: truth; blue: prior;
red: post−oco2;green: post−gosat
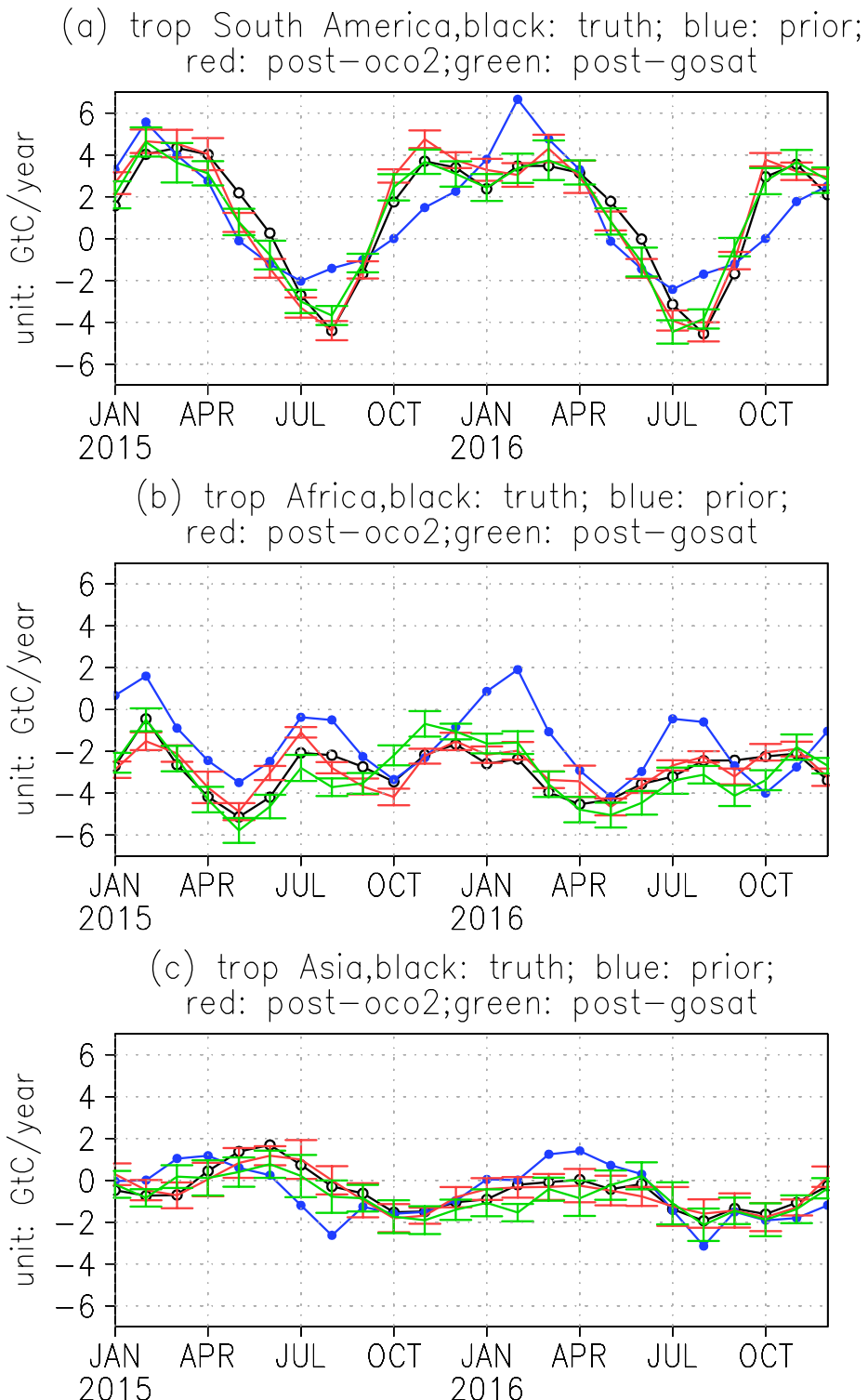
Figure S10 The prior (blue), truth (black), and the posterior fluxes and their uncertainties (error bars) from OSSEs based on ACOS-GOSAT (green) and OCO-2 (red) sampling and observation error statistics over tropical South America (a), tropical Africa (b), and tropical Asia (c).

(a) the number of aircraft observations at
each 4x5 between 2000m and 3000m in 2011

(b) the number of aircraft observations at
each 4x5 between 2000m and 3000m in 2015

(c) the number of flask observations at
each 4x5 in 2011

(d) the number of flask observations at
each 4x5 in 2015
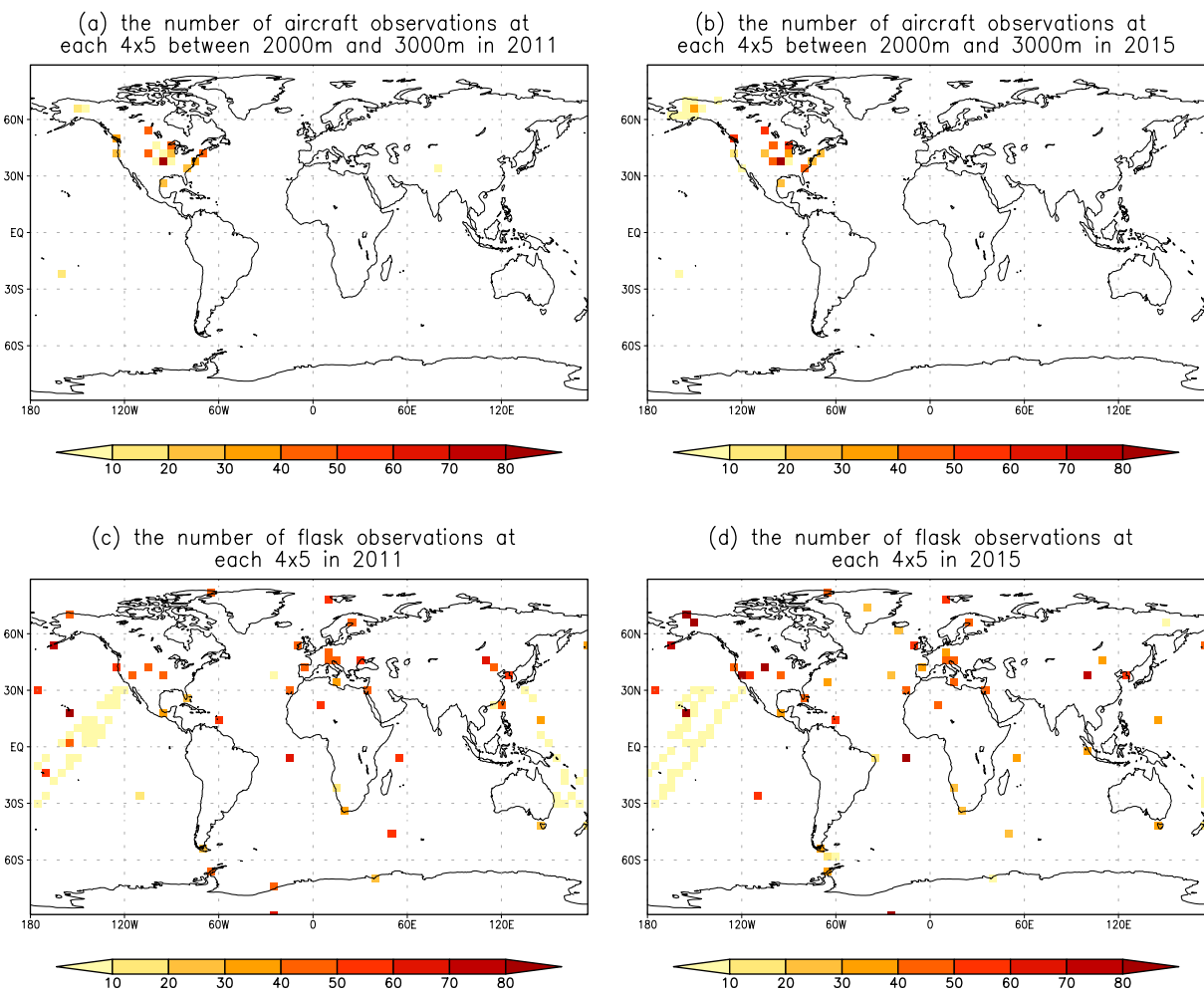
Figure S11 a, b: The total number of aircraft observations at each 4°5° grid point between 2000 meters and 3000 meters in 2011 and 2015 respectively; c, d: The total number of flask observations at each 4° 5° grid point in 2011 and 2015 respectively.

24
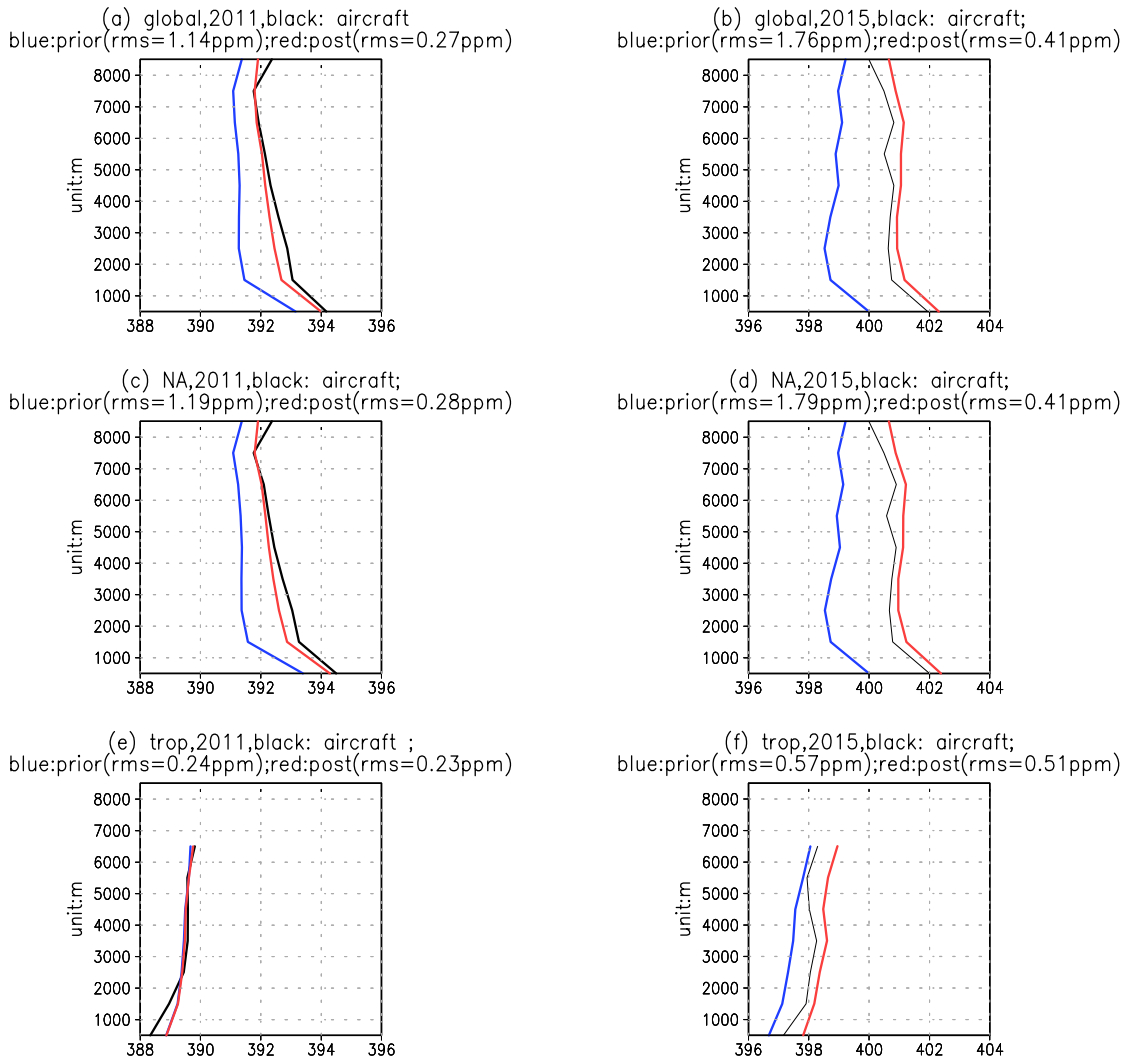
Figure S12 The inter-comparison among aircraft CO2 observations (black), model simulated CO2 observations forced by the prior fluxes (blue), and posterior fluxes (red) over the globe (a, b), the North America (c, d), and the tropics (e, f) for year 2011 (left column) and 2015 (right column). The RMS errors for the prior CO2 concentration and posterior CO2 concentration are included in the title.
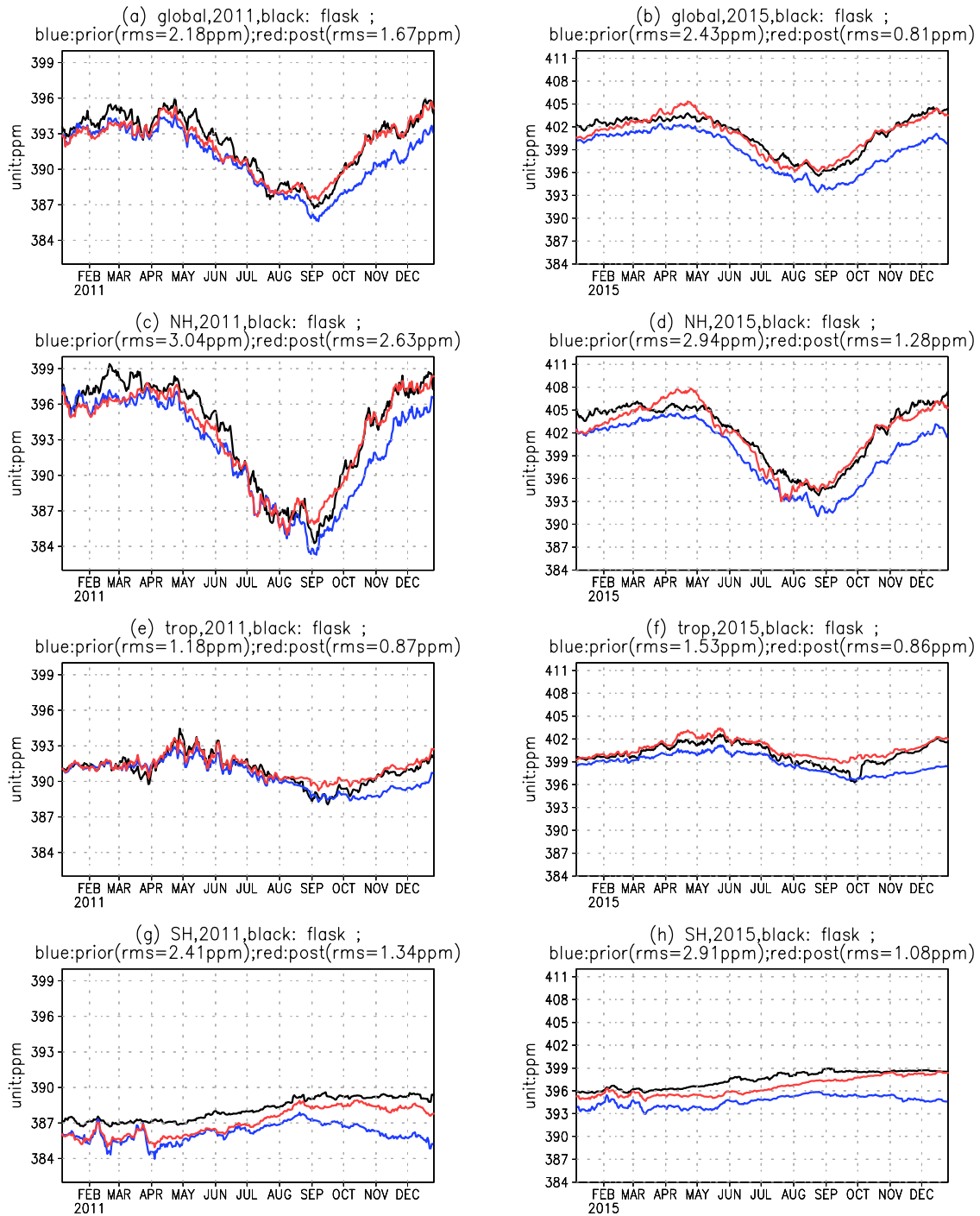
Figure S13 The inter-comparison among surface flask CO2 observations (black), model simulated CO2 observations forced by prior fluxes (blue), and posterior fluxes (red) over the globe (a, b), the NH (c, d), the tropics (e, f), and the SH (g, h) for year 2011 (left column) and 2015 (right column). The RMS errors for the prior CO2 concentration and posterior CO2 concentration are included in the title.

Table S1. List of flux magnitudes and atmospheric CO2 growth rate for 2011 and 2015.
Unit: GtC/year.

year	Fossil Fuel	Land use land change (*19*, GCP, 2016)	Ocean Flux	Prior NBE (include land use)	Posterior NBE (include land use)	Total posterior flux	NOAA atmospheric CO2 growth rate (*19,* GCP, 2016)	Airborne fraction
2011	9.62±0.15	0.91±0.50	-2.70±0.11	-3.50±0.74	-3.46±0.59	3.46±0.65	3.58±0.20	0.34
2015	9.86±0.17	1.32±0.50	-2.98±0.11	-3.50±0.74	-0.47±0.53	6.41±0.64	6.30±0.20	0.56

References and Notes

1. N. Zeng, A. Mariotti, P. Wetzel, Terrestrial mechanisms of interannual CO_2 variability. *Global Biogeochem. Cycles* **19**, GB1016 (2005). doi:10.1029/2004GB002273

2. P. M. Cox, D. Pearson, B. B. Booth, P. Friedlingstein, C. Huntingford, C. D. Jones, C. M. Luke, Sensitivity of tropical carbon to climate change constrained by carbon dioxide variability. *Nature* **494**, 341–344 (2013). doi:10.1038/nature11882 Medline

3. W. Wang, P. Ciais, R. R. Nemani, J. G. Canadell, S. Piao, S. Sitch, M. A. White, H. Hashimoto, C. Milesi, R. B. Myneni, Variations in atmospheric CO_2 growth rates coupled with tropical temperature. *Proc. Natl. Acad. Sci. U.S.A.* **110**, 13061–13066 (2013). doi:10.1073/pnas.1219683110 Medline

4. P. M. Cox, R. A. Betts, C. D. Jones, S. A. Spall, I. J. Totterdell, Acceleration of global warming due to carbon-cycle feedbacks in a coupled climate model. *Nature* **408**, 184–187 (2000). doi:10.1038/35041539 Medline

5. P. Friedlingstein, P. Cox, R. Betts, L. Bopp, W. von Bloh, V. Brovkin, P. Cadule, S. Doney, M. Eby, I. Fung, G. Bala, J. John, C. Jones, F. Joos, T. Kato, M. Kawamiya, W. Knorr, K. Lindsay, H. D. Matthews, T. Raddatz, P. Rayner, C. Reick, E. Roeckner, K.-G. Schnitzler, R. Schnur, K. Strassmann, A. J. Weaver, C. Yoshikawa, N. Zeng, Climate–carbon cycle feedback analysis: Results from the C^4MIP Model Intercomparison. *J. Clim.* **19**, 3337–3353 (2006). doi:10.1175/JCLI3800.1

6. I. Y. Fung, S. C. Doney, K. Lindsay, J. John, Evolution of carbon sinks in a changing climate. *Proc. Natl. Acad. Sci. U.S.A.* **102**, 11201–11206 (2005). doi:10.1073/pnas.0504949102 Medline

7. P. Ciais, A. J. Dolman, A. Bombelli, R. Duren, A. Peregon, P. J. Rayner, C. Miller, N. Gobron, G. Kinderman, G. Marland, N. Gruber, F. Chevallier, R. J. Andres, G. Balsamo, L. Bopp, F.-M. Bréon, G. Broquet, R. Dargaville, T. J. Battin, A. Borges, H. Bovensmann, M. Buchwitz, J. Butler, J. G. Canadell, R. B. Cook, R. DeFries, R. Engelen, K. R. Gurney, C. Heinze, M. Heimann, A. Held, M. Henry, B. Law, S. Luyssaert, J. Miller, T. Moriyama, C. Moulin, R. B. Myneni, C. Nussli, M. Obersteiner, D. Ojima, Y. Pan, J.-D. Paris, S. L. Piao, B. Poulter, S. Plummer, S. Quegan, P. Raymond, M. Reichstein, L. Rivier, C. Sabine, D. Schimel, O. Tarasova, R. Valentini, R. Wang, G. van der Werf, D. Wickland, M. Williams, C. Zehner, Current systematic carbon-cycle observations and the need for implementing a policy-relevant carbon observing system. *Biogeosciences* **11**, 3547–3602 (2014). doi:10.5194/bg-11-3547-2014

8. D. Schimel, R. Pavlick, J. B. Fisher, G. P. Asner, S. Saatchi, P. Townsend, C. Miller, C. Frankenberg, K. Hibbard, P. Cox, Observing terrestrial ecosystems and the carbon cycle from space. *Glob. Chang. Biol.* **21**, 1762–1776 (2015). doi:10.1111/gcb.12822 Medline

9. J. B. Fisher, M. Sikka, S. Sitch, P. Ciais, B. Poulter, D. Galbraith, J.-E. Lee, C. Huntingford, N. Viovy, N. Zeng, A. Ahlström, M. R. Lomas, P. E. Levy, C. Frankenberg, S. Saatchi, Y. Malhi, African tropical rainforest net carbon dioxide fluxes in the twentieth century. *Philos. Trans. R. Soc. Lond. B Biol. Sci.* **368**, 20120376 (2013). doi:10.1098/rstb.2012.0376 Medline

10. D. Schimel, B. B. Stephens, J. B. Fisher, Effect of increasing CO_2 on the terrestrial carbon cycle. *Proc. Natl. Acad. Sci. U.S.A.* **112**, 436–441 (2015). doi:10.1073/pnas.1407302112 Medline

11. W. R. L. Anderegg, A. P. Ballantyne, W. K. Smith, J. Majkut, S. Rabin, C. Beaulieu, R. Birdsey, J. P. Dunne, R. A. Houghton, R. B. Myneni, Y. Pan, J. L. Sarmiento, N. Serota, E. Shevliakova, P. Tans, S. W. Pacala, Tropical nighttime warming as a dominant driver of variability in the terrestrial carbon sink. *Proc. Natl. Acad. Sci. U.S.A.* **112**, 15591–15596 (2015). Medline

12. D. Crisp, C. E. Miller, P. L. DeCola, NASA Orbiting Carbon Observatory: Measuring the column averaged carbon dioxide mole fraction from space. *J. Appl. Remote Sens.* **2**, 023508 (2008). doi:10.1117/1.2898457

13. S. D. Polade, D. W. Pierce, D. R. Cayan, A. Gershunov, M. D. Dettinger, The key role of dry days in changing regional climate and precipitation regimes. *Sci. Rep.* **4**, 4364 (2014). doi:10.1038/srep04364 Medline

14. J. D. Neelin, C. Chou, H. Su, Tropical drought regions in global warming and El Niño teleconnections. *Geophys. Res. Lett.* **30**, 2275 (2003). doi:10.1029/2003GL018625

15. R. Chadwick, P. Good, G. Martin, D. P. Rowell, Large rainfall changes consistently projected over substantial areas of tropical land. *Nat. Clim. Chang.* **6**, 177–181 (2016).

16. Y. Malhi, J. Wright, Spatial patterns and recent trends in the climate of tropical rainforest regions. *Philos. Trans. R. Soc. Lond. B Biol. Sci.* **359**, 311–329 (2004). doi:10.1098/rstb.2003.1433 Medline

17. R. A. Betts, C. D. Jones, J. R. Knight, R. F. Keeling, J. J. Kennedy, El Niño and a record CO_2 rise. *Nat. Clim. Chang.* **6**, 806–810 (2016). doi:10.1038/nclimate3063

18. T. F. Keenan, I. C. Prentice, J. G. Canadell, C. A. Williams, H. Wang, M. Raupach, G. J. Collatz, Recent pause in the growth rate of atmospheric CO_2 due to enhanced terrestrial carbon uptake. *Nat. Commun.* **7**, 13428 (2016). doi:10.1038/ncomms13428 Medline

19. C. Le Quéré, R. M. Andrew, J. G. Canadell, S. Sitch, J. I. Korsbakken, G. P. Peters, A. C. Manning, T. A. Boden, P. P. Tans, R. A. Houghton, R. F. Keeling, S. Alin, O. D. Andrews, P. Anthoni, L. Barbero, L. Bopp, F. Chevallier, L. P. Chini, P. Ciais, K. Currie, C. Delire, S. C. Doney, P. Friedlingstein, T. Gkritzalis, I. Harris, J. Hauck, V. Haverd, M. Hoppema, K. Klein Goldewijk, A. K. Jain, E. Kato, A. Körtzinger, P. Landschützer, N. Lefèvre, A. Lenton, S. Lienert, D. Lombardozzi, J. R. Melton, N. Metzl, F. Millero, P. M. S. Monteiro, D. R. Munro, J. E. M. S. Nabel, S. Nakaoka, K. O'Brien, A. Olsen, A. M. Omar, T. Ono, D. Pierrot, B. Poulter, C. Rödenbeck, J. Salisbury, U. Schuster, J. Schwinger, R. Séférian, I. Skjelvan, B. D. Stocker, A. J. Sutton, T. Takahashi, H. Tian, B. Tilbrook, I. T. van der Laan-Luijkx, G. R. van der Werf, N. Viovy, A. P. Walker, A. J. Wiltshire, S. Zaehle, Global carbon budget 2016. *Earth Syst. Sci. Data* **8**, 605–649 (2016). doi:10.5194/essd-8-605-2016

20. A. Chatterjee, M. M. Gierach, A. J. Sutton, R. A. Feely, D. Crisp, A. Eldering, M. R. Gunson, C. W. O'Dell, B. B. Stephens, D. S. Schimel, Influence of El Niño on atmospheric CO_2 over the tropical Pacific Ocean: Findings from NASA's OCO-2 mission. *Science* **358**, eaam5776 (2017).

21. B. Poulter, D. Frank, P. Ciais, R. B. Myneni, N. Andela, J. Bi, G. Broquet, J. G. Canadell, F. Chevallier, Y. Y. Liu, S. W. Running, S. Sitch, G. R. van der Werf, Contribution of semi-arid ecosystems to interannual variability of the global carbon cycle. *Nature* **509**, 600–603 (2014). doi:10.1038/nature13376 Medline

22. J. A. Marengo, C. A. Nobre, J. Tomasella, M. D. Oyama, G. Sampaio de Oliveira, R. de Oliveira, H. Camargo, L. M. Alves, I. F. Brown, The drought of Amazonia in 2005. *J. Clim.* **21**, 495–516 (2008). doi:10.1175/2007JCLI1600.1 Medline

23. J. A. Marengo, J. Tomasella, L. M. Alves, W. R. Soares, D. A. Rodriguez, The drought of 2010 in the context of historical droughts in the Amazon region. *Geophys. Res. Lett.* **38**, L12703 (2011). doi:10.1029/2011GL047436

24. T. Yokota, Y. Yoshida, N. Eguchi, Y. Ota, T. Tanaka, H. Watanabe, S. Maksyutov, Global concentrations of CO_2 and CH_4 retrieved from GOSAT: First preliminary results. *Sci. Online Lett. Atmos.* **5**, 160–163 (2009). doi:10.2151/sola.2009-041

25. J. Liu, K. W. Bowman, M. Lee, D. K. Henze, N. Bousserez, H. Brix, G. James Collatz, D. Menemenlis, L. Ott, S. Pawson, D. Jones, R. Nassar, Carbon monitoring system flux estimation and attribution: Impact of ACOS-GOSAT X_{CO2} sampling on the inference of terrestrial biospheric sources and sinks. *Tellus B Chem. Phys. Meterol.* **66**, 22486 (2014). doi:10.3402/tellusb.v66.22486

26. J. Liu, K. W. Bowman, M. Lee, Comparison between the Local Ensemble Transform Kalman Filter (LETKF) and 4D-Var in atmospheric CO_2 flux inversion with the Goddard Earth Observing System-Chem model and the observation impact diagnostics from the LETKF. *J. Geophys. Res. Atmos.* **121**, 13,066–13,087 (2016). doi:10.1002/2016JD025100

27. K. W. Bowman, J. Liu, A. A. Bloom, N. C. Parazoo, M. Lee, Z. Jiang, D. Menemenlis, M. M. Gierach, G. J. Collatz, K. R. Gurney, D. Wunch, Global and Brazilian carbon response to El Niño Modoki 2011–2010. *Earth Space Sci.* **4**, ea000204 (2017). doi:10.1002/2016ea000204

28. See supplementary materials.

29. A. Eldering, P. O. Wennberg, D. Crisp, D. Schimel, M. R. Gunson, A. Chatterjee, J. Liu, F. M. Schwandner, Y. Sun, C. W. O'Dell, C. Frankenberg, T. Taylor, B. Fisher, G. B. Osterman, D. Wunch, J. Hakkarainen, J. Tamminen, B. Weir, The Orbiting Carbon Observatory-2 early science investigations of regional carbon dioxide fluxes, *Science* **358**, eaam5745 (2017).

30. D. Wunch, G. C. Toon, J.-F. L. Blavier, R. A. Washenfelder, J. Notholt, B. J. Connor, D. W. T. Griffith, V. Sherlock, P. O. Wennberg, The total carbon column observing network. *Philos. Trans. A Math. Phys. Eng. Sci.* **369**, 2087–2112 (2011). doi:10.1098/rsta.2010.0240 Medline

31. C. Frankenberg, J. B. Fisher, J. Worden, G. Badgley, S. S. Saatchi, J.-E. Lee, G. C. Toon, A. Butz, M. Jung, A. Kuze, T. Yokota, New global observations of the terrestrial carbon cycle from GOSAT: Patterns of plant fluorescence with gross primary productivity. *Geophys. Res. Lett.* **38**, L17706 (2011). doi:10.1029/2011GL048738

32. N. C. Parazoo, K. Bowman, J. B. Fisher, C. Frankenberg, D. B. A. Jones, A. Cescatti, O. Pérez-Priego, G. Wohlfahrt, L. Montagnani, Terrestrial gross primary production inferred

from satellite fluorescence and vegetation models. *Glob. Chang. Biol.* **20**, 3103–3121 (2014). doi:10.1111/gcb.12652 Medline

33. N. Parazoo, E. Barnes, J. Worden, A. B. Harper, K. B. Bowman, C. Frankenberg, S. Wolf, M. Litvak, T. F. Keenan, Influence of ENSO and the NAO on terrestrial carbon uptake in the Texas–northern Mexico region. *Global Biogeochem. Cycles* **29**, 1247–1265 (2015). doi:10.1002/2015GB005125

34. M. N. Deeter *et al*., Vertical resolution and information content of CO profiles retrieved by MOPITT. *Geophys. Res. Lett.* **31**, L15112 (2004). doi:10.1029/2004GL020235

35. Z. Jiang, Z. Liu, T. Wang, C. S. Schwartz, H.-C. Lin, F. Jiang, Probing into the impact of 3DVAR assimilation of surface PM_{10} observations over China using process analysis. *J. Geophys. Res. Atmos.* **118**, 6738–6749 (2013). doi:10.1002/jgrd.50495

36. C. E. Stockwell, T. Jayarathne, M. A. Cochrane, K. C. Ryan, E. I. Putra, B. H. Saharjo, A. D. Nurhayati, I. Albar, D. R. Blake, I. J. Simpson, E. A. Stone, R. J. Yokelson, Field measurements of trace gases and aerosols emitted by peat fires in Central Kalimantan, Indonesia, during the 2015 El Niño. *Atmos. Chem. Phys.* **16**, 11711–11732 (2016). doi:10.5194/acp-16-11711-2016

37. Y. Yin, P. Ciais, F. Chevallier, G. R. van der Werf, T. Fanin, G. Broquet, H. Boesch, A. Cozic, D. Hauglustaine, S. Szopa, Y. Wang, Variability of fire carbon emissions in equatorial Asia and its nonlinear sensitivity to El Niño. *Geophys. Res. Lett.* **43**, 10,472–10,479 (2016). doi:10.1002/2016GL070971

38. V. Huijnen, M. J. Wooster, J. W. Kaiser, D. L. A. Gaveau, J. Flemming, M. Parrington, A. Inness, D. Murdiyarso, B. Main, M. van Weele, Fire carbon emissions over maritime southeast Asia in 2015 largest since 1997. *Sci. Rep.* **6**, 26886 (2016). doi:10.1038/srep26886 Medline

39. S. E. Page, F. Siegert, J. O. Rieley, H.-D. V. Boehm, A. Jaya, S. Limin, The amount of carbon released from peat and forest fires in Indonesia during 1997. *Nature* **420**, 61–65 (2002). doi:10.1038/nature01131 Medline

40. J. C. Jiménez-Muñoz, C. Mattar, J. Barichivich, A. Santamaría-Artigas, K. Takahashi, Y. Malhi, J. A. Sobrino, Gv. Schrier, Record-breaking warming and extreme drought in the Amazon rainforest during the course of El Niño 2015–2016. *Sci. Rep.* **6**, 33130 (2016). doi:10.1038/srep33130 Medline

41. S. L. Lewis, P. M. Brando, O. L. Phillips, G. M. F. van der Heijden, D. Nepstad, The 2010 Amazon drought. *Science* **331**, 554 (2011). doi:10.1126/science.1200807 Medline

42. C. E. Doughty, D. B. Metcalfe, C. A. J. Girardin, F. F. Amézquita, D. G. Cabrera, W. H. Huasco, J. E. Silva-Espejo, A. Araujo-Murakami, M. C. da Costa, W. Rocha, T. R. Feldpausch, A. L. M. Mendoza, A. C. L. da Costa, P. Meir, O. L. Phillips, Y. Malhi, Drought impact on forest carbon dynamics and fluxes in Amazonia. *Nature* **519**, 78–82 (2015). doi:10.1038/nature14213 Medline

43. C. B. Alden, J. B. Miller, L. V. Gatti, M. M. Gloor, K. Guan, A. M. Michalak, I. T. van der Laan-Luijkx, D. Touma, A. Andrews, L. S. Basso, C. S. C. Correia, L. G. Domingues, J. Joiner, M. C. Krol, A. I. Lyapustin, W. Peters, Y. P. Shiga, K. Thoning, I. R. van der Velde, T. T. van Leeuwen, V. Yadav, N. S. Diffenbaugh, Regional atmospheric CO_2

inversion reveals seasonal and geographic differences in Amazon net biome exchange. *Glob. Chang. Biol.* **22**, 3427–3443 (2016). [doi:10.1111/gcb.13305](doi:10.1111/gcb.13305) Medline

44. L. V. Gatti, M. Gloor, J. B. Miller, C. E. Doughty, Y. Malhi, L. G. Domingues, L. S. Basso, A. Martinewski, C. S. C. Correia, V. F. Borges, S. Freitas, R. Braz, L. O. Anderson, H. Rocha, J. Grace, O. L. Phillips, J. Lloyd, Drought sensitivity of Amazonian carbon balance revealed by atmospheric measurements. *Nature* **506**, 76–80 (2014). doi:10.1038/nature12957 Medline

45. I. T. van der Laan-Luijkx, I. R. van der Velde, M. C. Krol, L. V. Gatti, L. G. Domingues, C. S. C. Correia, J. B. Miller, M. Gloor, T. T. van Leeuwen, J. W. Kaiser, C. Wiedinmyer, S. Basu, C. Clerbaux, W. Peters, Response of the Amazon carbon balance to the 2010 drought derived with CarbonTracker South America. *Global Biogeochem. Cycles* **29**, 1092–1108 (2015). [doi:10.1002/2014GB005082](doi:10.1002/2014GB005082)

46. S. L. Lewis, P. M. Brando, O. L. Phillips, G. M. F. van der Heijden, D. Nepstad, The 2010 Amazon drought. *Science* **331**, 554 (2011). doi:10.1126/science.1200807 Medline

47. P. Ciais, M. Williams, S. L. Piao, J. Chave, C. M. Ryan, M. Henry, P. Brender, R. Valentini, The carbon balance of Africa: Synthesis of recent research studies. *Phil. Trans. R. Soc. A* **369**, 2038–2057 (2011). doi:10.1098/rsta.2010.0328

48. X. Wang, S. Piao, P. Ciais, P. Friedlingstein, R. B. Myneni, P. Cox, M. Heimann, J. Miller, S. Peng, T. Wang, H. Yang, A. Chen, A two-fold increase of carbon cycle sensitivity to tropical temperature variations. *Nature* **506**, 212–215 (2014). doi:10.1038/nature12915 Medline

49. Y. Malhi, J. T. Roberts, R. A. Betts, T. J. Killeen, W. Li, C. A. Nobre, Climate change, deforestation, and the fate of the Amazon. *Science* **319**, 169–172 (2008). doi:10.1126/science.1146961 Medline

50. P. B. Duffy, P. Brando, G. P. Asner, C. B. Field, Projections of future meteorological drought and wet periods in the Amazon. *Proc. Natl. Acad. Sci. U.S.A.* **112**, 13172–13177 (2015). doi:10.1073/pnas.1421010112 Medline

51. A. Russo, A. F. Marchese, J. Sillmann, G. Immé, When will unusual heat waves become normal in a warming Africa?. *Environ. Res. Lett.* **11**, 054016 (2016). [doi:10.1088/1748-9326/11/5/054016](doi:10.1088/1748-9326/11/5/054016) Medline

52. K. Steinkamp, N. Gruber, Decadal trends of ocean and land carbon fluxes from a regional joint ocean-atmosphere inversion. *Global Biogeochem. Cycles* **29**, 2108–2126 (2015). [doi:10.1002/2014GB004907](doi:10.1002/2014GB004907)

53. R. J. W. Brienen, O. L. Phillips, T. R. Feldpausch, E. Gloor, T. R. Baker, J. Lloyd, G. Lopez-Gonzalez, A. Monteagudo-Mendoza, Y. Malhi, S. L. Lewis, R. Vásquez Martinez, M. Alexiades, E. Álvarez Dávila, P. Alvarez-Loayza, A. Andrade, L. E. O. C. Aragão, A. Araujo-Murakami, E. J. M. M. Arets, L. Arroyo, G. A. Aymard C, O. S. Bánki, C. Baraloto, J. Barroso, D. Bonal, R. G. A. Boot, J. L. C. Camargo, C. V. Castilho, V. Chama, K. J. Chao, J. Chave, J. A. Comiskey, F. Cornejo Valverde, L. da Costa, E. A. de Oliveira, A. Di Fiore, T. L. Erwin, S. Fauset, M. Forsthofer, D. R. Galbraith, E. S. Grahame, N. Groot, B. Hérault, N. Higuchi, E. N. Honorio Coronado, H. Keeling, T. J. Killeen, W. F. Laurance, S. Laurance, J. Licona, W. E. Magnussen, B. S. Marimon, B. H.

Marimon-Junior, C. Mendoza, D. A. Neill, E. M. Nogueira, P. Núñez, N. C. Pallqui Camacho, A. Parada, G. Pardo-Molina, J. Peacock, M. Peña-Claros, G. C. Pickavance, N. C. A. Pitman, L. Poorter, A. Prieto, C. A. Quesada, F. Ramírez, H. Ramírez-Angulo, Z. Restrepo, A. Roopsind, A. Rudas, R. P. Salomão, M. Schwarz, N. Silva, J. E. Silva-Espejo, M. Silveira, J. Stropp, J. Talbot, H. ter Steege, J. Teran-Aguilar, J. Terborgh, R. Thomas-Caesar, M. Toledo, M. Torello-Raventos, R. K. Umetsu, G. M. F. van der Heijden, P. van der Hout, I. C. Guimarães Vieira, S. A. Vieira, E. Vilanova, V. A. Vos, R. J. Zagt, Long-term decline of the Amazon carbon sink. *Nature* **519**, 344–348 (2015). doi:10.1038/nature14283 Medline

54. H. Ivancic, L. P. Koh, Evolution of sustainable palm oil policy in Southeast Asia. *Cogent Environ. Sci.* **2**, 1195032 (2016). doi:10.1080/23311843.2016.1195032

55. W. R. Anderegg, C. Schwalm, F. Biondi, J. J. Camarero, G. Koch, M. Litvak, K. Ogle, J. D. Shaw, E. Shevliakova, A. P. Williams, A. Wolf, E. Ziaco, S. Pacala, Pervasive drought legacies in forest ecosystems and their implications for carbon cycle models. *Science* **349**, 528–532 (2015). doi:10.1126/science.aab1833 Medline

56. P. M. Brando, D. C. Nepstad, E. A. Davidson, S. E. Trumbore, D. Ray, P. Camargo, Drought effects on litterfall, wood production and belowground carbon cycling in an Amazon forest: Results of a throughfall reduction experiment. *Philos. Trans. R. Soc. Lond. B Biol. Sci.* **363**, 1839–1848 (2008). doi:10.1098/rstb.2007.0031 Medline

57. T. L. Powell, D. R. Galbraith, B. O. Christoffersen, A. Harper, H. M. A. Imbuzeiro, L. Rowland, S. Almeida, P. M. Brando, A. C. L. da Costa, M. H. Costa, N. M. Levine, Y. Malhi, S. R. Saleska, E. Sotta, M. Williams, P. Meir, P. R. Moorcroft, Confronting model predictions of carbon fluxes with measurements of Amazon forests subjected to experimental drought. *New Phytol.* **200**, 350–365 (2013). doi:10.1111/nph.12390 Medline

58. M. Reichstein, M. Bahn, P. Ciais, D. Frank, M. D. Mahecha, S. I. Seneviratne, J. Zscheischler, C. Beer, N. Buchmann, D. C. Frank, D. Papale, A. Rammig, P. Smith, K. Thonicke, M. van der Velde, S. Vicca, A. Walz, M. Wattenbach, Climate extremes and the carbon cycle. *Nature* **500**, 287–295 (2013). doi:10.1038/nature12350 Medline

59. J. Zscheischler, M. Reichstein, J. von Buttlar, M. Mu, J. T. Randerson, M. D. Mahecha, Carbon cycle extremes during the 21st century in CMIP5 models: Future evolution and attribution to climatic drivers. *Geophys. Res. Lett.* **41**, 8853–8861 (2014). doi:10.1002/2014GL062409

60. D. Frank, M. Reichstein, M. Bahn, K. Thonicke, D. Frank, M. D. Mahecha, P. Smith, M. van der Velde, S. Vicca, F. Babst, C. Beer, N. Buchmann, J. G. Canadell, P. Ciais, W. Cramer, A. Ibrom, F. Miglietta, B. Poulter, A. Rammig, S. I. Seneviratne, A. Walz, M. Wattenbach, M. A. Zavala, J. Zscheischler, Effects of climate extremes on the terrestrial carbon cycle: Concepts, processes and potential future impacts. *Glob. Chang. Biol.* **21**, 2861–2880 (2015). doi:10.1111/gcb.12916 Medline

61. H. Kreft, W. Jetz, Global patterns and determinants of vascular plant diversity. *Proc. Natl. Acad. Sci. U.S.A.* **104**, 5925–5930 (2007). doi:10.1073/pnas.0608361104 Medline

62. S. L. Lewis, B. Sonké, T. Sunderland, S. K. Begne, G. Lopez-Gonzalez, G. M. F. van der Heijden, O. L. Phillips, K. Affum-Baffoe, T. R. Baker, L. Banin, J.-F. Bastin, H.

Beeckman, P. Boeckx, J. Bogaert, C. De Cannière, E. Chezeaux, C. J. Clark, M. Collins, G. Djagbletey, M. N. K. Djuikouo, V. Droissart, J.-L. Doucet, C. E. N. Ewango, S. Fauset, T. R. Feldpausch, E. G. Foli, J.-F. Gillet, A. C. Hamilton, D. J. Harris, T. B. Hart, T. de Haulleville, A. Hladik, K. Hufkens, D. Huygens, P. Jeanmart, K. J. Jeffery, E. Kearsley, M. E. Leal, J. Lloyd, J. C. Lovett, J.-R. Makana, Y. Malhi, A. R. Marshall, L. Ojo, K. S.-H. Peh, G. Pickavance, J. R. Poulsen, J. M. Reitsma, D. Sheil, M. Simo, K. Steppe, H. E. Taedoumg, J. Talbot, J. R. D. Taplin, D. Taylor, S. C. Thomas, B. Toirambe, H. Verbeeck, J. Vleminckx, L. J. T. White, S. Willcock, H. Woell, L. Zemagho, Above-ground biomass and structure of 260 African tropical forests. *Philos. Trans. R. Soc. Lond. B Biol. Sci.* **368**, 20120295 (2013). doi:10.1098/rstb.2012.0295 Medline

63. I. J. Polonsky, D. M. O'Brien, J. B. Kumer, C. W. O'Dell, Performance of a geostationary mission, geoCARB, to measure CO_2, CH_4 and CO column-averaged concentrations. *Atmos. Meas. Tech.* **7**, 959–981 (2014). doi:10.5194/amt-7-959-2014

64. M. M. Rienecker et al., The GEOS-5 data assimilation systemdocumentation of versions 5.0.1 and 5.1.0, and 5.2.0 (NASA Tech. Rep. Series on Global Modeling and Data Assimilation, PublicationTM-2008-104606, NASA, 2008), vol. 27.

65. M. Parrington, D. B. A. Jones, K. W. Bowman, L. W. Horowitz, A. M. Thompson, D. W. Tarasick, J. C. Witte, Estimating the summertime tropospheric ozone distribution over North America through assimilation of observations from the Tropospheric Emission Spectrometer. *J. Geophys. Res.* **113**, D18307 (2008). doi:10.1029/2007JD009341

66. K. A. Masarie, W. Peters, A. R. Jacobson, P. P. Tans, ObsPack: A framework for the preparation, delivery, and attribution of atmospheric greenhouse gas measurements. *Earth Syst. Sci. Data* **6**, 375–384 (2014). doi:10.5194/essd-6-375-201467. N. Deutscher *et al.*, TCCON data from Bialystok, Poland, Release GGG2014R1, TCCON data archive, hosted by Carbon Dioxide Information Analysis Center (CDIAC) (2014). doi:10.14291/tccon.ggg2014.bialystok01.R1/1183984

68. J. Notholt, *et al.*, TCCON data from Bremen, Germany, Release GGG2014R0. TCCON data archive, hosted by Carbon Dioxide Information Analysis Center (CDIAC) (2014). doi:10.14291/tccon.ggg2014.bremen01.R0/1149275

69. D. W. T. Griffith, *et al.*, TCCON data from Darwin, Australia, Release GGG2014R0. TCCON data archive, hosted by Carbon Dioxide Information Analysis Center (CDIAC) (2014). doi:10.14291/tccon.ggg2014.darwin01.R0/1149290

70. K. Strong, *et al.*, TCCON data from Eureka, Canada, Release GGG2014R0. TCCON data archive, hosted by Carbon Dioxide Information Analysis Center (CDIAC) (2014). doi:10.14291/tccon.ggg2014.eureka01.R0/1149271

71. R. Sussmann and M. Rettinger, TCCON data from Garmisch, Germany, Release GGG2014R0. TCCON data archive, hosted by Carbon Dioxide Information Analysis Center (CDIAC) (2014). doi:10.14291/tccon.ggg2014.garmisch01.R0/1149299

72. K. Shiomi *et al.*, TCCON data from Saga, Japan, Release GGG2014R0. TCCON data archive, hosted by Carbon Dioxide Information Analysis Center (CDIAC) (2014). doi:10.14291/tccon.ggg2014.saga01.R0/1149283

73. F. Hase, *et al.*, TCCON data from Karlsruhe, Germany, Release GGG2014R1. TCCON data

archive, hosted by Carbon Dioxide Information Analysis Center (CDIAC) (2014). doi:10.14291/tccon.ggg2014.karlsruhe01.R1/1182416

74. V. Sherlock *et al.*, TCCON data from Lauder, New Zealand, 125HR, Release GGG2014R0. TCCON data archive, hosted by Carbon Dioxide Information Analysis Center (CDIAC), (2014). doi:10.14291/tccon.ggg2014.lauder02.R0/1149298

75. P. O. Wennberg, *et al.*, TCCON data from Lamont, Oklahoma, USA, Release GGG2014R1. TCCON data archive, hosted by Carbon Dioxide Information Analysis Center (CDIAC), (2014). doi:10.14291/tccon.ggg2014.lamont01.R1/1255070

76. T. Warneke *et al.*, TCCON data from Orleans, France, Release GGG2014R0. TCCON data archive, hosted by Carbon Dioxide Information Analysis Center (CDIAC) (2014). doi:10.14291/tccon.ggg2014.orleans01.R0/1149276

77. P. O. Wennberg, *et al.*, TCCON data from Park Falls, Wisconsin, USA, Release GGG2014R0. TCCON data archive, hosted by Carbon Dioxide Information Analysis Center (CDIAC) (2014). doi:10.14291/tccon.ggg2014.parkfalls01.R0/1149161

78. R. Kivi, *et al.*, TCCON data from Sodankyla, Finland, Release GGG2014R0. TCCON data archive, hosted by Carbon Dioxide Information Analysis Center (CDIAC) (2014). doi:10.14291/tccon.ggg2014.sodankyla01.R0/1149280

79. I. Morino *et al.*, TCCON data from Tsukuba, Ibaraki, Japan, 125HR, Release GGG2014R1. TCCON data archive, hosted by Carbon Dioxide Information Analysis Center (CDIAC) (2014). doi:10.14291/tccon.ggg2014.tsukuba02.R1/1241486

80. D. W. T. Griffith, *et al.*, TCCON data from Wollongong, Australia, Release GGG2014R0. TCCON data archive, hosted by Carbon Dioxide Information Analysis Center (CDIAC) (2014). doi:10.14291/tccon.ggg2014.wollongong01.R0/1149291

81. D. Wunch, P. O. Wennberg, G. Osterman, B. Fisher, B. Naylor, C. M. Roehl, C. O'Dell, L. Mandrake, C. Viatte, M. Kiel, D. W. T. Griffith, N. M. Deutscher, V. A. Velazco, J. Notholt, T. Warneke, C. Petri, M. De Maziere, M. K. Sha, R. Sussmann, M. Rettinger, D. Pollard, J. Robinson, I. Morino, O. Uchino, F. Hase, T. Blumenstock, D. G. Feist, S. G. Arnold, K. Strong, J. Mendonca, R. Kivi, P. Heikkinen, L. Iraci, J. Podolske, P. W. Hillyard, S. Kawakami, M. K. Dubey, H. A. Parker, E. Sepulveda, O. E. García, Y. Te, P. Jeseck, M. R. Gunson, D. Crisp, A. Eldering, Comparisons of the Orbiting Carbon Observatory-2 (OCO-2) X_{CO2} measurements with TCCON. *Atmos. Meas. Tech.* **10**, 2209–2238 (2017). doi:10.5194/amt-10-2209-2017

82. P. Xie, P. A. Arkin, Global precipitation: A 17-year monthly analysis based on gauge observations, satellite estimates, and numerical model outputs. *Bull. Am. Meteorol. Soc.* **78**, 2539–2558 (1997). doi:10.1175/1520-0477(1997)078<2539:GPAYMA>2.0.CO;2

83. D. P. Dee, S. M. Uppala, A. J. Simmons, P. Berrisford, P. Poli, S. Kobayashi, U. Andrae, M. A. Balmaseda, G. Balsamo, P. Bauer, P. Bechtold, A. C. M. Beljaars, L. van de Berg, J. Bidlot, N. Bormann, C. Delsol, R. Dragani, M. Fuentes, A. J. Geer, L. Haimberger, S. B. Healy, H. Hersbach, E. V. Hólm, L. Isaksen, P. Kållberg, M. Köhler, M. Matricardi, A. P. McNally, B. M. Monge-Sanz, J.-J. Morcrette, B.-K. Park, C. Peubey, P. de Rosnay, C. Tavolato, J.-N. Thépaut, F. Vitart, The ERA-Interim reanalysis: Configuration and

performance of the data assimilation system. *Q. J. R. Meteorol. Soc.* **137**, 553–597 (2011). [doi:10.1002/qj.828](doi:10.1002/qj.828)

84. D. Wunch, P. O. Wennberg, J. Messerschmidt, N. C. Parazoo, G. C. Toon, N. M. Deutscher, G. Keppel-Aleks, C. M. Roehl, J. T. Randerson, T. Warneke, J. Notholt, The covariation of Northern Hemisphere summertime CO_2 with surface temperature in boreal regions. *Atmos. Chem. Phys.* **13**, 9447–9459 (2013). [doi:10.5194/acp-13-9447-2013](doi:10.5194/acp-13-9447-2013)

85. J. T. Randerson, M. V. Thompson, T. J. Conway, I. Y. Fung, C. B. Field, The contribution of terrestrial sources and sinks to trends in the seasonal cycle of atmospheric carbon dioxide. *Global Biogeochem. Cycles* **11**, 535–560 (1997). [doi:10.1029/97GB02268](doi:10.1029/97GB02268)

86. A. Eldering, C. W. O'Dell, P. O. Wennberg, D. Crisp, M. R. Gunson, C. Viatte, C. Avis, A. Braverman, R. Castano, A. Chang, L. Chapsky, C. Cheng, B. Connor, L. Dang, G. Doran, B. Fisher, C. Frankenberg, D. Fu, R. Granat, J. Hobbs, R. A. M. Lee, L. Mandrake, J. McDuffie, C. E. Miller, V. Myers, V. Natraj, D. O'Brien, G. B. Osterman, F. Oyafuso, V. H. Payne, H. R. Pollock, I. Polonsky, C. M. Roehl, R. Rosenberg, F. Schwandner, M. Smyth, V. Tang, T. E. Taylor, C. To, D. Wunch, J. Yoshimizu, The Orbiting Carbon Observatory-2: First 18 months of science data products. *Atmos. Meas. Tech.* **10**, 549–563 (2017). [doi:10.5194/amt-10-549-2017](doi:10.5194/amt-10-549-2017)

87. J. Liu, I. Fung, E. Kalnay, J.-S. Kang, E. T. Olsen, and L. Chen, Simultaneous assimilation of AIRS Xco_2 and meteorological observations in a carbon climate model with an ensemble Kalman filter, J. Geophys. Res., 117, D05309, (2012), [doi:10.1029/2011JD016642](doi:10.1029/2011JD016642).

88. J. R. Worden, G. Doran, S. Kulawik, A. Eldering, D. Crisp, C. Frankenberg, C. O'Dell, K. Bowman, Evaluation and attribution of OCO-2 X_{CO2} uncertainties. *Atmos. Meas. Tech.* **10**, 2759–2771 (2017). [doi:10.5194/amt-10-2759-2017](doi:10.5194/amt-10-2759-2017)

89. C. Frankenberg, S. S. Kulawik, S. C. Wofsy, F. Chevallier, B. Daube, E. A. Kort, C. O'Dell, E. T. Olsen, G. Osterman, Using airborne HIAPER Pole-to-Pole Observations (HIPPO) to evaluate model and remote sensing estimates of atmospheric carbon dioxide. *Atmos. Chem. Phys.* **16**, 7867–7878 (2016). [doi:10.5194/acp-16-7867-2016](doi:10.5194/acp-16-7867-2016)

90. S. S. Kulawik, D. Wunch, C. O'Dell, C. Frankenberg, M. Reuter, T. Oda, F. Chevallier, V. Sherlock, M. Buchwitz, G. Osterman, C. E. Miller, P. O. Wennberg, D. Griffith, I. Morino, M. K. Dubey, N. M. Deutscher, J. Notholt, F. Hase, T. Warneke, R. Sussmann, J. Robinson, K. Strong, M. Schneider, M. De Mazière, K. Shiomi, D. G. Feist, L. T. Iraci, J. Wolf, Consistent evaluation of ACOS-GOSAT, BESD-SCIAMACHY, CarbonTracker, and MACC through comparisons to TCCON. *Atmos. Meas. Tech.* **9**, 683–709 (2016). [doi:10.5194/amt-9-683-2016](doi:10.5194/amt-9-683-2016)

91. D. Menemenlis, J.-M. Campin, P. Heimbach, C. Hill, T. Lee, A. Nguyen, M. Schodlok, H. Zhang, ECCO2: High resolution global ocean and sea ice data synthesis. *Mercator Ocean Quarterly Newsletter.* **31**, 13–21 (2008).

92. S. Dutkiewicz, M. Follows, J. Bragg, Modeling the coupling of ocean ecology and biogeochemistry. *Global Biogeochem. Cycles* **23**, GB4017 (2009). [doi:10.1029/2008GB003405](doi:10.1029/2008GB003405)

93. S. Asefi-Najafabady, P. J. Rayner, K. R. Gurney, A. McRobert, Y. Song, K. Coltin, J. Huang, C. Elvidge, K. Baugh, A multiyear, global gridded fossil fuel CO_2 emission data product:

Evaluation and analysis of results. *J. Geophys. Res.* **119**, 10,213–10,231 (2014). doi:10.1002/2013JD021296

94. C. Le Quéré, R. J. Andres, T. Boden, T. Conway, R. A. Houghton, J. I. House, G. Marland, G. P. Peters, G. R. van der Werf, A. Ahlström, R. M. Andrew, L. Bopp, J. G. Canadell, P. Ciais, S. C. Doney, C. Enright, P. Friedlingstein, C. Huntingford, A. K. Jain, C. Jourdain, E. Kato, R. F. Keeling, K. Klein Goldewijk, S. Levis, P. Levy, M. Lomas, B. Poulter, M. R. Raupach, J. Schwinger, S. Sitch, B. D. Stocker, N. Viovy, S. Zaehle, N. Zeng, The global carbon budget 1959–2011. *Earth Syst. Sci. Data* **5**, 165–185 (2013). doi:10.5194/essd-5-165-2013

95. S. Sitch, P. Friedlingstein, N. Gruber, S. D. Jones, G. Murray-Tortarolo, A. Ahlström, S. C. Doney, H. Graven, C. Heinze, C. Huntingford, S. Levis, P. E. Levy, M. Lomas, B. Poulter, N. Viovy, S. Zaehle, N. Zeng, A. Arneth, G. Bonan, L. Bopp, J. G. Canadell, F. Chevallier, P. Ciais, R. Ellis, M. Gloor, P. Peylin, S. L. Piao, C. Le Quéré, B. Smith, Z. Zhu, R. Myneni, Recent trends and drivers of regional sources and sinks of carbon dioxide. *Biogeosciences* **12**, 653–679 (2015). doi:10.5194/bg-12-653-2015

96. E. Kalnay, M. Kanamitsu, R. Kistler, W. Collins, D. Deaven, L. Gandin, M. Iredell, S. Saha, G. White, J. Woollen, Y. Zhu, A. Leetmaa, R. Reynolds, M. Chelliah, W. Ebisuzaki, W. Higgins, J. Janowiak, K. C. Mo, C. Ropelewski, J. Wang, R. Jenne, D. Joseph, The NCEP/NCAR 40-year reanalysis project. *Bull. Am. Meteorol. Soc.* **77**, 437–471 (1996). doi:10.1175/1520-0477(1996)077<0437:TNYRP>2.0.CO;2

97. CarbonTracker Team, Compilation of near real time atmospheric carbon dioxide data provided by National Oceanic and Atmospheric Administration (NOAA) and Environment Canada (EC), obspack_co2_1_NRT_v3.1_2016-09-06 (NOAA Earth System Research Laboratory, Global Monitoring Division, 2016). doi:10.15138/G3VC71